universität wien

MASTERARBEIT / MASTER'S THESIS

Titel der Masterarbeit / Title of the Master's Thesis

Chirality Sorting and Characterization of Ultra-Low Boron-Doped SWCNTs

verfasst von / submitted by

Alice Kern, BSc

angestrebter akademischer Grad / in partial fulfilment of the requirements for the degree of

Master of Science (MSc)

Wien, 2025 / Vienna, 2025

Studienkennzahl lt. Studienblatt / degree programme code as it appears on the student record sheet:	UA 066 876
Studienrichtung lt. Studienblatt / degree programme as it appears on the student record sheet:	Masterstudium Physik
Betreut von / Supervisor:	Univ. Prof. Dr. Paola Ayala

Acknowledgements

I would like to express my deepest gratitude to my thesis advisor, Univ. Prof. Dr. Paola Ayala, for her invaluable guidance, support, and encouragement throughout this journey. Her insightful advice and expertise have been instrumental in shaping my research and completing this thesis. Beyond her academic support, she has been an inspiring role model, demonstrating dedication and passion for science and gender equality for women in physics qualities that I deeply admire.
I am also profoundly thankful to Dido Denier van der Gon, BSc MSc, whose constant support and insightful advice were crucial throughout this project. Sharing an office with her was a privilege.

I want to thank my grandparents who have only shown me love and support, since the day I took my first breath. While they didn't have the opportunity to attend higher education, their support and love made this possible — this is for you as much as for me. I want to thank my sister, Hanni, who's been my biggest supporter, all her life, you are my better half. I want to thank my fiancé - you are everything to me.
Most importantly, I want to thank my mum, without whose support nothing in my life would have been possible. She filled my and my sister's lives with books and art and music providing me with role models from Sarah Jessica Parka to Donna Leon. She never gave me any idea that I couldn't do whatever I wanted or be whomever I wanted, for that I will be forever grateful. I owe her everything, this is for you.

Abstract

This Master's thesis focuses on the characterization of ultra-low boron-doped single-walled carbon nanotubes (CBx-SWNTs) using advanced spectroscopic techniques to assess the physical properties and the quality of the CBx-SWNTs sample. Substitutional doping of SWCNTs with B is a promising approach to tune their electronic and optical properties. However, the purification and sorting processes presents a significant challenge, due to the chemical complexities of B containing compounds.
The thesis examines CBx-SWCNTs samples who have been purified using five different purification pathways and then sorted by Density Gradient Ultracentrifugation (DGU). The potential for chirality sorting using DGU and the different purification pathways for low doped CBx-SWNTs have been evaluated. The results demonstrate a successful purification pathway, achieving a low damage index (I_D/I_G ratio of ~ 0.17), which indicates high material quality. The sorting process reveals a predominance of the semiconducting chiralities (6,5), (8,4), and (8,6), which are highly relevant for optoelectronic applications. Moreover, this thesis provides a purification pathway combined with DGU, resulting in a sample exhibiting photoluminescence (PL) from only three chiralities, which is a step forward towards single chirality sorting.
While promising advancements are highlighted, the impact of B-doping on the PL and absorption spectroscopy response remains inconclusive and requires further investigation. Future research should focus on optimizing surfactant combinations and integrating additional sorting techniques to improve chirality isolation. This thesis contributes valuable insights into the characterization of different purification methods and the sorting of functionalized SWNTs, advancing their potential for practical applications.
In summary, this Master thesis is organized into five chapters, starting with a comprehensive 'Motivation' section that outlines the driving factors and significance of this work. Then, 'Background', which provides a detailed synopsis of the methodologies and principles underlying the optical and electronic properties and synthesis of CBx-SWCNT. The 'Material and Methods' chapter elaborates on the materials used and the experimental approaches employed, highlighting the sample preparation and the steps taken towards chirality sorting of CBx-SWNTs with DGU.
In the 'Optical spectroscopy Results' chapter the found impact of the purification methods on the quality of the sample will be described as well the results of the chirality sorting are shown. These findings demonstrate the potential for obtaining a substantial amount of specific semiconducting nanotubes via purification and a single sorting step. Finally, the 'Conclusion and Outlook' chapter provides a summary of the drawn conclusions from this work and discusses future research directions. These include suggestions for optimizing sorting processes of CBx-SWNTs.

Kurzzusammenfassung

Diese Masterarbeit befasst sich mit der Charakterisierung von ultraniedrig Bor dotierten einwändigen Kohlenstoffnanoröhren (CBx-SWNTs) mit fortschrittlichen spektroskopischen Methoden zur Bewertung der physikalischen Eigenschaften und der Qualität von den CBx-SWCNT Proben. Die Substitutionsdotierung von SWCNTs mit Bor ist ein vielversprechender Ansatz um ihre elektronischen und optischen Eigenschaften zu verändern, doch die Reinigung und Sortierung stellt aufgrund der chemischen Komplexität borhaltiger Verbindungen eine große Herausforderung dar.
Die Arbeit untersucht das Potenzial von fünf verschiedenen Reinigungsverfahren und die Chiralitätssortierung mittels Dichtegradienten-Ultrazentrifugation (DGU).
Die Ergebnisse zeigen einen erfolgreiche Reinigungsmethode, die einen niedrigen Defektindex (I_D/I_G-Verhältnis von $\sim 0,17$) erreicht, was auf eine hohe Materialqualität hindeutet. Der Sortierprozess zeigt eine Dominanz der halbleitenden Chiralitäten (6,5), (8,4) und (8,6), die für optoelektronische Anwendungen von großer Bedeutung sind. Darüber hinaus wird in dieser Arbeit ein Reinigungsverfahren in Kombination mit der DGU-Sortierung vorgestellt, welche zu einer Probe führt, die vor allem das PL-Signal von drei Chiralitäten zeigt. Dies ist ein Fortschritt in Richtung selektiver Sortierung einzelner Chiralitäten.
Während vielversprechende Fortschritte hervorgehoben werden, bleiben die Auswirkungen der Bor-Dotierung auf die Photolumineszenz (PL) und die Absorptionsspektroskopie unschlüssig und bedarf weiterer Untersuchungen. Künftige Forschungsarbeiten sollten sich auf die Optimierung von Tensidkombinationen und die Integration zusätzlicher Sortierungsverfahren zur Verbesserung der Chiralitätsisolierung konzentrieren. Diese Arbeit liefert wertvolle Einblicke in die Charakterisierung verschiedener Reinigungsmethoden und Sortierung von funktionalisierten CBx-SWNTs, welches ihr Potenzial für praktische Anwendungen fördert.
Zusammenfassend ist diese Masterarbeit in fünf Kapitel gegliedert, beginnend mit dem Kapitel „Motivation“, in dem die treibenden Faktoren und die Bedeutung dieser Arbeit ausführulich dargelegt werden. Dann folgt das Kapitel „Background“, das einen detaillierten Überblick über die Methoden und Grundsätze gibt, die den optischen und elektronischen Eigenschaften und der Synthese von CBx-SWCNT zugrunde liegen. Im Kapitel „Materials and Methods“ werden die verwendeten Proben und die experimentellen Ansätze beschrieben, wobei der Process für die Chiralitätssortierung mit DGU hervorgehoben wird. In dem Kapitel „Optical spectroscopy Result“ werden die gefundenen Auswirkungen der Reinigungsmethoden auf die Qualität der Probe beschrieben und die Ergebnisse der Chiralitätssortierung dargestellt. Diese Ergebnisse zeigen das Potenzial, mit einem Reinigungsprocess und einem einzigen Sortierschritt eine beträchtliche Menge spezifischer halbleitender Nanoröhren zu erhalten. Das Kapitel „Conclusion and Outlook“ fasst die Schlussfolgerungen aus dieser Arbeit zusammen und erörtert

zukünftige Forschungsrichtungen. Dazu gehören auch Vorschläge zur Optimierung der Sortierprozesse von CBx-SWNTs.

Contents

List of Figures

1 Motivation

Single-walled carbon nanotubes (SWCNTs) are one-dimensional structures of sp^2-hybridized carbon atoms arranged in a honeycomb lattice that is rolled up into a tube. They were discovered by Iijima and Ichihashi in 1991[10] [11], and since then, they have garnered significant interest due to their mechanical, electronic, and optical properties, as well as their potential applications across different scientific fields.
Over the last decades tremendous efforts have been made to exploit their properties. Among various modifications of pristine SWCNTs, substitutional doping of SWCNTs with heteroatoms has proven to be a promising pathway to tailor their features. While the doping with Nitrogen (N) has been extensively studied, doping with Boron (B) is less explored. In this thesis the focus will lie solely on B-doped SWCNTs (CBx-SWCNTs)[12]. Due to the similar atomic size and electronic configuration of B, it is a suitable substitution for C. Its incorporation into the graphene lattice introduces acceptor states in the electronic band structure, this happens already at very low doping concentrations. Therefore the introduction of B influences the electronic behavior of SWCNTs, enabling new functionalities such as p-type conductivity[13]. Additionally, B doping can cause subtle changes in vibrational properties, detectable through Raman spectroscopy, such as shifts in the radial breathing modes (RBM) and the G-band. However, the substitution of B in SWCNTs is not always uniform, and the formation of nanodomains can complicate the characterization and optimization of their properties[14] [15].
The synthesis of CBx-SWCNTs is still a challenge since traditional methods, such as arc discharge and laser ablation, face limitations in controlling doping levels. However, chemical vapor deposition (CVD), is a widely used technique for synthesizing pristine SWCNTs and has shown promising upscalability. The Tailored Hybrid Structures research group at the University of Vienna, where my thesis work was conducted, has pioneered a high vacuum CVD-based method for producing high-quality CBx-SWCNTs with a very narrow diameter distribution and diameter sizes comparable to pristine SWCNTs, produced with higher temperature methods like arc discharge or laser ablation. This method utilizes merely the vapor pressure of a liquid feedstock as C and B source[16]-[17].
An essential aspect of working with CBx-SWNTs is their purification process after synthesis. Unlike pristine SWCNTs, which already have well-established purification protocols, the presence of B in the lattice complicates the cleaning process[12]. This thesis reviews five different purification pathways and how well these approaches can be used to remove impurities while preserving the structural and electronic integrity of CBx-SWNTs. Purification is a crucial part for enabling the application of CBx-SWCNTs in sensitive fields such as bio-materials and optoelectronics, where material purity directly influences the performance. Another critical challenge is the isolation of distinct CBx-SWNTs chirality species. Since, the chirality of the nanotube determines its electronic and optical

properties, it is crucial to be able to sort for specific chirality species, as electronically homogeneous SWCNTs are required for certain applications[18]. Progress has already been made in the controlled growth of CBx-SWCNTs, but the low yield and low purity sparked interest in post synthesis sorting[19]. One way to do this is Density Gradient Ultracentrifugation (DGU). It is a key technique employed for both purification and sorting, as it utilizes the subtle differences in buoyant densities of the chiralities. This allows for the separation of metallic and semiconducting SWCNTs, as well as sorting by diameter and chirality, with high precision. For CBx-SWCNTs, DGU is particularly advantageous due to its non-destructive nature, which allows for separation while preserving their structural integrity[20]. Chirality-specific sorting of CBx-SWCNTs is essential to realizing their full potential. Consequently, a low-cost but high-purity purification and separation method is crucial for the industry application of CBx-SWCNTs.[21].
My thesis addresses these aspects through an indirect approach, focusing on detailed spectroscopic studies to evaluate the efficiency of different purification pathways and subsequent sorting with DGU. The samples have been characterized after purification with Raman spectroscopy, afterwards DGU was used to disperse and sort the CBx-SWCNTs, followed by characterization with optical absorption and photoluminescence spectroscopy. These spectroscopic methods have been central for assessing the quality of the final product and understanding the effects of the processing methods.

2 Background

This chapter provides a general introduction to SWCNTs, their optical, electronic properties and the underlying physics of the optical methods employed, as well as an overview of CBx-SWNTs and their synthesis. The sections 2.1 to 2.4 largely follow the chapters on Structure and Symmetry, Electronic Properties of Carbon Nanotubes and Optical Properties from the book Carbon Nanotubes: Basic Concepts and Physical Properties by Thomsen, Maultzsch, and Reich (2004)[4].

2.1 Atomic Structure and Geometry of SWCNTs

SWCNT can be imagined as a graphene sheet that has been rolled up to form a closed cylinder (Fig. 2.1). The basis vectors of the hexagonal graphene lattice are $\vec{a}_1 = \frac{a}{2}(3, \sqrt{3})$ and $\vec{a}_2 = \frac{a}{2}(3, -\sqrt{3})$, and $a = 1.42$Å is the $C - C$ bond length[2].
The roll-up vector $\vec{C}$, which is the circumference of the tube is given by

$$\vec{C} = n_1\vec{a}_1 + n_2\vec{a}_2 \equiv (n_1, n_2) \tag{2.1}$$

where (n_1, n_2) is a pair of integers that uniquely define a particular nanotube and are referred to as the chiral indices[1]. The diameter of the nanotube can be calculated using following equation

$$d_t = \frac{L}{\pi} = \left(\frac{\sqrt{3}}{\pi}\right) a\sqrt{n_1^2 + n_1 n_2 + n_2^2} \tag{2.2}$$

with $L = \sqrt{C \cdot C}$, the length of the chiral vector. The chiral angle of a carbon nanotube is defined as the angle between the vectors $\vec{a}_1$ and $\vec{C}$ and is expressed as

$$cos\theta = \frac{\vec{a_1} \cdot \vec{C}}{|\vec{a_1}| \cdot |\vec{C}|} = \frac{n_1 + n_2/2}{\sqrt{n_1^2 + n_1 n_2 + n_2^2}} \tag{2.3}$$

For every carbon nanotube with an angle θ of $0° < \theta < 30°$ and chiral indices (n_1, n_2), a tube with an angle θ of $30° < \theta < 60°$ and chiral indices (n_2, n_1) exists. However, the helix of the graphene lattice will change from right-handed to left-handed. SWCNTs with indices $(n, 0)$ and chiral angle $\theta = 0°$ are referred to as zig-zag tubes due the presence of a zig-zag pattern along the circumference (see 2.1) and SWCNTs with indices (n_1, n_1) and a chiral angle of $\theta = 30°$ are called armchair tubes. Zig-zag and armchair tubes are two special cases of SWCNTs and are called achiral tubes in comparison to all other chiral SWCNTs.

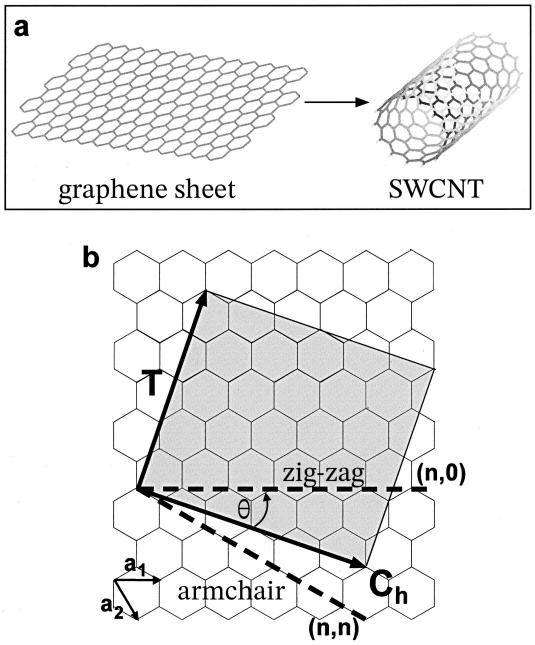

Figure 2.1: a) The image of a 2D graphene sheet rolled up to form a SWCNT. b) 2D graphene sheet with the corresponding lattice vectors a_1 and a_2 and the circumference vector $\vec{C}$. Adapted from [1].

The bonds between the immediate three C neighbors in a graphene sheet are given by

$$\vec{r}_1 = a(0, 1) \tag{2.4}$$

$$\vec{r}_2 = a(\frac{\sqrt{3}}{2}, \frac{1}{2}) \tag{2.5}$$

$$\vec{r}_3 = a(-\frac{\sqrt{3}}{2}, -\frac{1}{2}). \tag{2.6}$$

They are equivalent, however their distances will change when the sheet is rolled up into a tube[2].
Another parameter of a SWCNT is the translational vector $\vec{T}$, which is the smallest graphene lattice vector oriented perpendicular to the roll-up vector $\vec{C}$. It can be derived from the magnitude of $\vec{C}$ and the highest common divisor of n_1 and n_2 and reads as follows

$$\vec{T} = -\frac{2n_2 + n_1}{nR}\vec{a}_1 - \frac{2n_1 + n_2}{nR}\vec{a}_2 \equiv (t_1, t_2) \tag{2.7}$$

and

$$T = |\vec{T}| = \frac{\sqrt{3(n_1^2 + n_1 n_2 + n_2^2)}}{nR} a_0 \tag{2.8}$$

If $(n_1 - n_2)/3n$ $R = 3$, otherwise $R = 1$, $a_0 = 1.42\text{Å}\sqrt{3} = 2.461\text{Å}$. The amount of carbon atoms within a unit cell can be derived from the ratio of the area of the cylinder surface

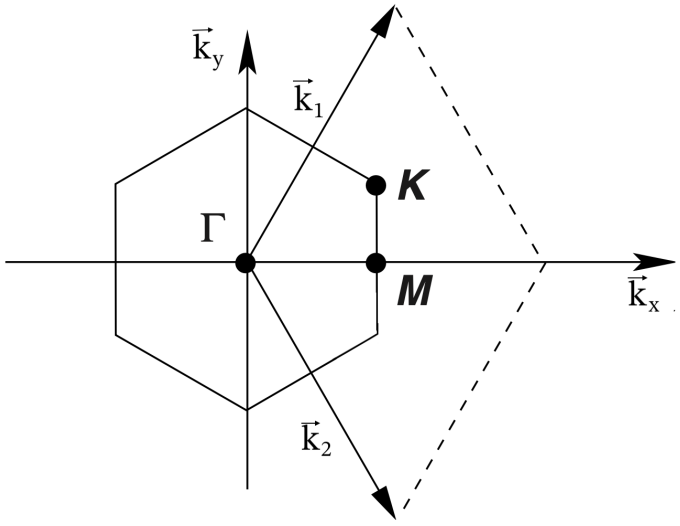

Figure 2.2: Brillouin zone of Graphene with the reciprocal lattice vectors and the high symmetry points(adapted from[2]).

and the area of the unit cell of graphene. The ratio yields the number N of graphene hexagons in the unit cell of the nanotube

$$N = \left| \frac{\vec{C} \times \vec{T}}{\vec{a}_1 \times \vec{a}_2} \right| = \frac{2(n_1^2 + n_1 n_2 + n_2^2)}{nR} \tag{2.9}$$

and because the unit cell of graphene encompasses two atoms, $2N$ will give the number of carbon atoms within the unit cell of the tube. $N = 2n$ for archiral nanotubes.

2.1.1 Brillouin Zone

The unit cell of graphene has been discussed in the section before, now the reciprocal lattice will be introduced. With the condition $\vec{a}_1 \cdot \vec{b_j} = 2\pi\sigma_{ij}$ the reciprocal lattice vectors can be obtained[3]. They read:

$$\vec{k}_1 = \left(\frac{\pi}{r_{2x}}, \frac{\pi}{r_{2y}} \right) = \frac{2\pi}{3a}(1, \sqrt{3}) \qquad \vec{k}_2 = \left(\frac{\pi}{r_{3x}}, \frac{\pi}{r_{3y}} \right) = \frac{2\pi}{3a}(1, -3) \tag{2.10}$$

The hexagonal Brillouin zone of graphene with the high symmetry points $\Gamma(k = 0)$, $K(k = 2\pi/\sqrt{3})$ and $M(k = \pi/a)$ and the reciprocal lattice vectors is illustrated Figure 2.2.
The high symmetry points represent points, which coincide with themselves after symmetry operations. In the z-direction, which is the direction of the tube axis, the reciprocal lattice vector k_z relates to the translational period a and is given by

$$k_z = \frac{2\pi}{a} \tag{2.11}$$

The nanotube will be assumed to be infinitely long, therefore k_z becomes continuous and any wavevector $k_\perp$ along the circumference of the tube will become quantized due to following boundary conditions:

$$m \cdot \lambda = |C| = \pi \cdot d \longleftrightarrow k_{\perp,m} = \frac{2\pi}{\lambda} = \frac{2\pi}{|C|} \cdot m = \frac{2}{d} \cdot m. \tag{2.12}$$

m an integer, can take the following values $\frac{-N}{2} + 1, ..., 0, 1, ..., \frac{N}{2}$. This means to satisfy he boundary condition, the wave function of a quasi-particle, has to exhibit a phase shift of an integer multiple of 2π around the nanotubes circumference and any other wavelengths cancel each other out due to interference. The number of atoms within an unit cell determine the maximum wave vector $|k_{\perp,m}|$. When projecting the carbon atoms onto the tubes circumference, uniformly spaced pairs of carbon atoms are formed. Therefore, four atoms are needed to define a wavelength. Then, the first Brillouin zone is composed of q lines, these line run parallel to the $z-$axis. Each line is spaced by $\Delta k = \frac{2\pi}{d}$ with k values between $-\frac{\pi}{a}, ..., \frac{2\pi}{a}$.

By applying following conditions

$$\begin{aligned} k_\perp \cdot C &= 2\pi \\ k \cdot C &= 0 \\ k_\perp \cdot T &= 0 \\ k_z \cdot T &= 2\pi \end{aligned} \tag{2.13}$$

the reciprocal lattice vector and the quantized wave vector can be determined as

$$k_\perp = \frac{2n_1 + n_2}{NnR} k_1 + \frac{2n_2 + n_1}{NnR} k_2 \tag{2.14}$$

$$k_z = -\frac{n_2}{N} k_1 + \frac{n_1}{N} k_2 \tag{2.15}$$

2.2 Electronic Properties of SWCNTs

The element carbon has 6 electrons, two electrons within $1sp^2$ orbital and four valence electrons in the $2s^2 2p^2$ orbital. The s and p orbitals hybridize, so that the energetic conditions favor the formation of covalent bonds in-plane of three of the electrons with the neighboring C atoms. These strong covalent bonds are primarily accounts for the elastic properties and binding energy of the graphene sheet[3].
The p_z orbital, points out of the sheet and exhibits off symmetry compared to the planar symmetry and therefore, cannot interact with the σ states. However, the p_z orbitals form

Dirac cones with $\pi-$electrons which can interact lateral with other p_z orbitals. They form de-localized π (bonding) and π^* (anti-bonding) network. This can bee seen in Figure 2.3. This de-localized π-network is mainly responsible for the electronic properties of the graphene sheet[3].

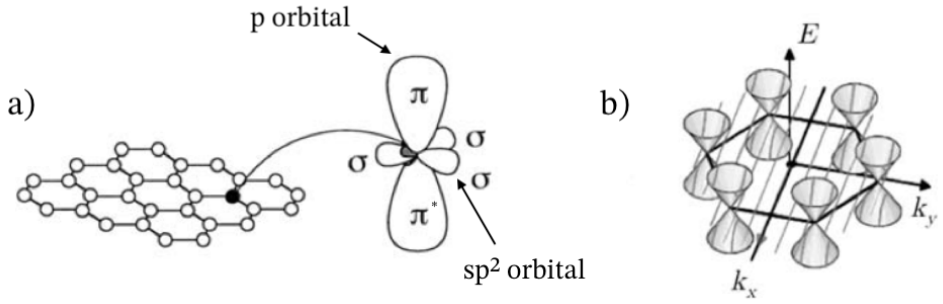

Figure 2.3: a) Depicted is the graphene sheet with the three σ orbitals and the π (bonding) and π^* (anti-bonding) orbitals. b) Illustration of the formed Dirac cones close to the Dirac points. (Figure adapted from [3]).

The tight-binding approximation is a common way to calculate the electronic band structure of graphene. This approximation considers electrons to be part of the atom and because of the small distances between the atoms the valence electrons can interact with each other. This interaction leads to a broadening of the electronic eigenstates and therefore, can be considered as a continuous band.
The structure of graphene was described before. When looking at the overlap of the p_z wavefunction with the s, p_x and p_y electrons it can be seen that, they have to be zero. The wavefunctions of sp^2 sheet are symmetric from points above and below, while the orbital p_z changes sign. When integrating over the entire lattice the overlap will vanish, since the negative and positive contribution will cancel each other out. Therefore,it is possible to look at the p_z electrons separately, without considering the interaction with other valence electrons. To calculate the electronic band structure of the π orbitals we first need to solve the Schrödinger‘s equation:

$$H\Psi(k) = E(k)\Psi(k) \tag{2.16}$$

The Hamiltonian, under the tight binding approximation, considers only nearest- and next-nearest-neighbor hopping, reads [2]:

$$H = -t \sum_{\langle i,j\rangle,\sigma} (a^\dagger_{\sigma,i} b^\dagger_{\sigma,j} + H.c) - t' \sum_{\langle\langle i,j\rangle\rangle,\sigma} (a^\dagger_{\sigma,i} a\sigma, i + b^\dagger_{\sigma,j} b_{\sigma,j} + H.c) \tag{2.17}$$

The operator $a^\dagger_{i,\sigma}$ creates, while $a_{i,\sigma}$ annihilates an electron with spin σ down or up on the site R_i on the sublattice A. The same is true for sublattice B. t denotes the energy required for nearest-neighbor hopping ($\approx 2.8eV$), while t' stands for the energy required for next-nearest hopping[2]. The energy bands derived from 2.17 will take the following

shape([22]):

$$E_{\pm}(k) = \pm t\sqrt{3 + f(k)} - t'f(k) \tag{2.18}$$

with

$$f(k_x, k_y) = 2cos(\sqrt{3}k_y a) + 4cos\left(\frac{\sqrt{3}}{2}k_y a\right) cos\left(\frac{3}{2}k_x a\right) \tag{2.19}$$

The minus in 2.18 denotes the lower band (π), while the plus denotes the upper band (π^*). In 2.19 it can be seen that if t' is zero, than the spectrum is symmetric at zero energy. However, if the values t' are finite this leads to the disruption of electron-hole symmetry, consequently rendering the bands asymmetric[2]. The Figure 2.4 depicts the tight-binding band structure of graphene. The Fermi level is located between the conducting and valence band, and they meet exactly at the high symmetry point K.

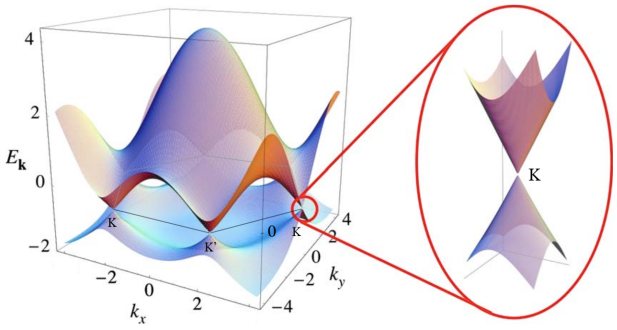

Figure 2.4: The tight binding band structure of the graphene lattice for finite values $t = 2.7eV$ and $t' = -0.2t$. The zoomed in part shows the energy bands close to the Dirac Point K(Figure adapted from [2]).

Graphene is classified as a semimetal, characterized by a Fermi surface consisting only of six discrete points in the k-space, which is the reason why SWCNTs can exhibit metallic or semiconducting behavior depending on their chirality.

After discussing the band structure of graphene, the electronic properties of SWCNTs can now be considered. Due to the periodic boundary conditions 2.12 any wavevector $k_\perp$ along the circumference becomes quantized and can only exhibit discrete values. However, the wavevectors associated with the direction of T will remain continuous for nanotubes of infinite length[2] [3]. If the allowed wave vectors are plotted onto the Brillouin zone, they manifest in multiple parallel lines (see Figure 2.5a). The orientation, quantity, inter-spacing and length of these k-vectors are determined by the specific chiral indices of the nanotube.

Zone-folding is one approach to calculate the electronic properties of carbon nanotube.

It is based on the idea that, the electronic band structure of the nanotube depends on the electronic energies of graphene along the allowed wavevectors. Most SWCNT are semiconducting and only a small fraction is metallic or quasi-metallic. In Figure 2.4 it can be seen that the valence and conducting band touch at the high symmetry point K. Therefore, if K is under the allowed wavevectors then the nanotube will exhibit metallic behavior, otherwise the nanotube will be semiconducting. Due to the boundary conditions the electronic states are limited to k-vectors, which meet the condition $k \cdot \vec{C} = 2\pi m$. The allowed k vectors of a general SWCNT (Figure 2.5a) around the high symmetry point K can be seen in Figure 2.5b). The K point is not allowed therefore it is a semiconducting nanotube.

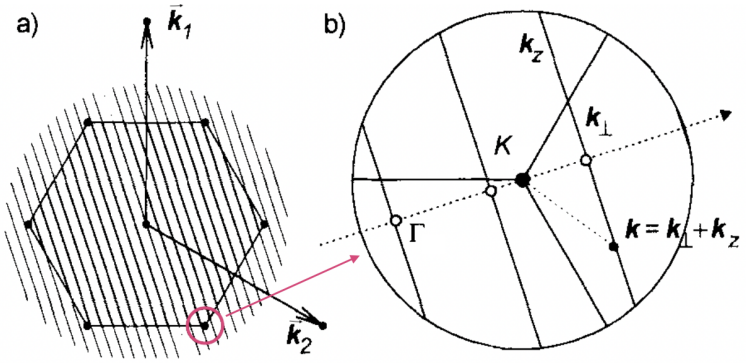

Figure 2.5: a) The allowed k-vectors plotted onto the Brillouin zone. b) Zoomed in view of the allowed wave vectors around the high symmetry point K. $k_\perp$ is the allowed wavevector around the circumference and k_z is continuous. The dotted line corresponds to points with $k_z = 0$ and to the Γ points on the tube (Figure adapted from [4]).

The the high symmetry point K is at $\frac{1}{3}(k_1 - k_2)$, therefore for a nanotube to be metallic following condition has to be true:

$$K \cdot c = 2\pi m = \frac{1}{3}(k_1 - k_2)(n_1 a_1 + n_2 a_2) = \frac{2\pi}{3}(n_1 - n_2) \tag{2.20}$$

or if

$$3m = n_1 - n_2 \tag{2.21}$$

This relation was first derived by Hamada et al.[23] and Saito et al. [24] independently. This states that a tube with $n_1 - n_2$ is a multiple of three is metallic. Projecting the K point along the tube axis yields the k_z at which the valence band and the conducting band meet within the Brillouin zone.

$$K \cdot \vec{T} = \frac{1}{3}(k_1 - k_2) \cdot \left(-\frac{2n_2 + n_1}{nR} a_1 + \frac{2n_1 + n_2}{nR} a_2 \right) = 2\pi k_z \tag{2.22}$$

k_z is continuous therefore the equation 2.22 becomes

$$K \cdot \vec{T} = -2\pi \frac{n_1 + n_2}{nR} \tag{2.23}$$

By subtracting reciprocal lattice vectors, we derive

$$k_z = \begin{cases} 0 & if \quad R = 1, \quad i.e., \quad (n_1 - n_2)/3n \quad not \quad integer. \\ 1/3 & if \quad R = 3, \quad i.e., \quad (n_1 - n_2)/3n \qquad integer. \end{cases} \tag{2.24}$$

Therefore, for metallic nanotubes with $R = 1$, the valence and the conducting band intersect at the high symmetry point Γ. However, if the tube has $R = 3$ then they intersect at only 1/3 of the k_z lattice vectors.
With the earlier introduced concepts of zone folding and the graphene tight-binding dispersion, the full band structure of carbon nanotubes can be derived . For this a well-known armchair tube of (10,10) chirality is considered.
The quantized wave vector and lattice vector are given by equation 2.14 and 2.15 and the electronic states at the point Γ are given by

$$k_\Gamma(m) = mk_\perp = m\left(\frac{2n_1 + n_2}{NnR}k_1 + \frac{2n_2 + n_1}{NnR}k_2\right) = m(\frac{1}{20}k_1 + \frac{1}{20}k_2) \tag{2.25}$$

the integer m goes from -10 to 9 under the consideration of this nanotube. This reflects the z-component of the angular momentum. In the units of the reciprocal lattice vectors the 1D Brillouin zone of the nanotube is given by

$$k_z = -\frac{n_2}{N}k_1 + \frac{n_1}{N}k_2 = -\frac{1}{2}k_1 + \frac{1}{2}k_2 \tag{2.26}$$

and represent the lines going from $k_\Gamma(m)$ to $k_\Gamma + k_z/2$. Plugging k_Γ and k_z into the nearest-neighbor expression for the band structure of graphene, then calculating the energies and plotting them as function of k_z, will give the band structure.

2.2.1 Density of States

Carbon nanotubes were already examined in the earlier sections as material similar to graphene with quantum confinement. The same will apply for this section. However, one major difference between graphene and carbon nanotubes is the reduced dimension and its effect. The density of states (DOS), gives the number of available electrons of an energy interval and strongly depends on the dimension of the system.
The density of states for i 1D electronic bands can be described by

$$n(E) = \frac{2}{q|k_z|}\sum_i \int dk_z \delta(k_z - k_i)\left|\frac{\partial E^{\pm}(k_\perp, k_z)}{\partial k_z}\right|^{-1} \tag{2.27}$$

$q|k_z|$ is the area of the Brillouin zone and k_i is described by $E - E^{\pm}(k_\perp, k_z)$. To find $\partial E^{\pm}/\partial k_z$ near the Fermi level the electronic bands will be approximated as straight lines close the high symmetry point K

$$E^{\pm}(k) = \mp\frac{\sqrt{3}}{2}a_0\gamma_0|k - k_F| \tag{2.28}$$

The permitted wave vectors are derived from $mk_\perp$ and a wave vector along k_z, therefore

$$|k - k_F| = \sqrt{\Delta k_m^2 + \Delta k_z^2} \tag{2.29}$$

Δk_m is quantized along the k_z direction, while Δk_z is parallel to k_z Therefore, Δk_z has continous values, while we need to find a quantized condition for Δk_m. This is can be done by projecting $(k - k_F)$ along $k_\perp$.

$$\Delta k_m = (k - k_F)\frac{k_\perp}{|k_\perp|} = \frac{4\pi}{3c}|3m - n_1 + n_2| \tag{2.30}$$

Inverting the partial derivative of 2.27 will give

$$\begin{aligned}\left|\frac{\partial E^{\pm}(k_\perp, k_Z)}{\partial}\right|^{-1} &= \frac{\sqrt{3}}{2}a_0\gamma_0\left|\frac{\partial\sqrt{\Delta k_m^2 + \Delta k_z^2}}{\partial k_z}\right|^{-1} \\ &= \frac{\sqrt{3}}{2}a_0\gamma_0\frac{|E^{\pm}|}{\sqrt{(E^{\pm})^2 - E_m^2}}\end{aligned} \tag{2.31}$$

with

$$E_m = \frac{\sqrt{3}}{2}a_0\gamma_0\Delta k_m = |3m - n_1 - n_2|\frac{a_0\gamma_0}{\sqrt{3}d}. \tag{2.32}$$

Plugging equation 2.31 into the equation 2.27 and then integrating over k_z will give a density of states $n(E)$

$$n(E) = \frac{8}{q|k_z|}\sum_{m=-\infty}^{\infty}\frac{2}{\sqrt{3}a_0\gamma_0}g(E, E_m). \tag{2.33}$$

$q|k_z| = 4\pi^2 d/\sqrt{3}a_0^2$ is the volume of the Brillouin zone, with that $n(E)$ can be written as

$$n(E) = \frac{4a_0}{\pi^2 d\gamma_0}\sum_{m=-\infty}^{\infty}g(E, E_m) \tag{2.34}$$

with

$$g(E_{Em}) = \begin{cases}|E|/\sqrt{E^2 - E_m^2} & |E| > |E_m| \\ 0 & |E| < |E_m|\end{cases}. \tag{2.35}$$

When $|E_m| = 0$, then is $g(E, E_m) = 1$ and it represents metallic tubes, the bands intersect at the Fermi Energy level. For $E_m \neq 0$ $g(E, E_m)$ is diverging at $E_m = E$, which is a characteristic of a critical point in a $1D$ system.

An extreme point in the electronic band structure gives rise to a divergence of the

density of states, these are called Van Hove singularities. Since the DOS is high at these singularities interactions (e.g. absorbance) are amplified[25].
The figure 2.6 shows the density of states of a semiconducting carbon nanotube, with the allowed optical transitions.

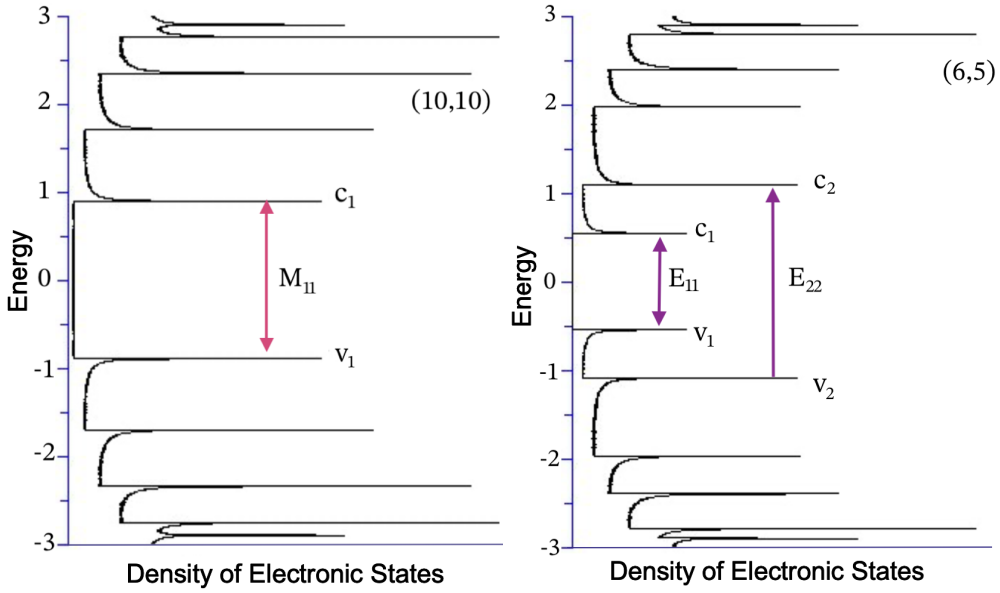

Figure 2.6: Density of states pattern in a semiconducting (6,5) and metallic (10,10) single-walled carbon nanotube. The sharp maxima are van Hove singularities and the arrows illustrate the optical absorption and emission transitions. (Figure adapted from [5]).

The van Hove singularities, dominate therefore many physical properties of the carbon nanotube[26]. Hence, analytical processes of the electronic structure can be simplified by investigating the optical transitions. According to the approximation by Mintmire and White [27], the nanotubes electronic band structure solely depends on the diameter. Each SWCNT has specific optical transition energies E_{ii} and these can be plottet as function of the diameter d_t. This relationship is captured in the Kataura plot (see Figure 2.7), a graphical tool that illustrates the relation of E_{ii} to the diameter of the SWCNTs. In the Kataura plot, the x-axis represents the nanotube diameter, while the y-axis corresponds to the energy values E_{ii}. The plot shows clusters of metallic and semiconducting nanotubes, with metallic nanotubes having near-zero band gaps (curvature effects can induce a small gap in quasi-metallic nanotubes) and semiconducting nanotubes exhibiting discrete energy gaps that decrease inversely with increasing diameter. By correlating the diameter to the electronic properties of SWCNTs, the Kataura plot plays a vital role in the characterization and analysis of SWCNTs[6].

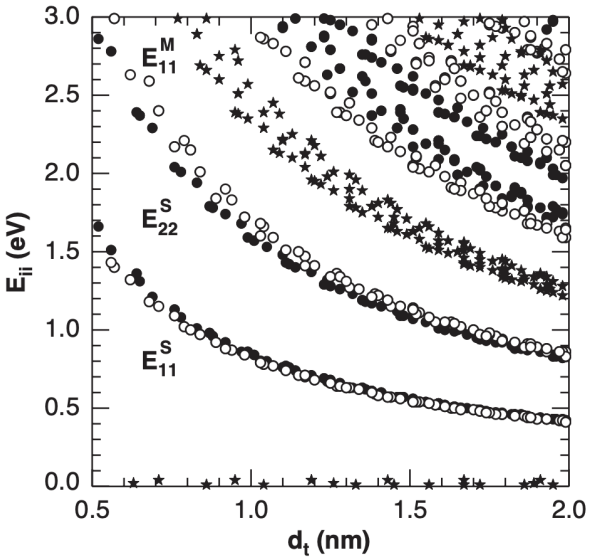

Figure 2.7: Kataura plot displaying the relationship of the electronic transition energies E_{ii} to the diameter d_t of SWCNT, derived with the tight binding approximation. Taken from [6].

2.3 Optical Properties of SWCNTs

In this section the optical properties of SWCNTs will be discussed. Absorbance and photoluminesence spectroscopy allow to probe electronic transitions of the SWCNT, while raman spectroscopy gives information about the vibrational properties.
When a phonon excites an electron from the valence band to a higher energy band, it is talked about optical absorbance. The photo-excited electron leaves behind an unoccupied state or a "hole" which behaves like positively charged particle. The photo-excited electron and the hole interact with each other by Coulomb interaction. An electron-hole pair or "exciton" is formed. The hole or the photo-excited electron can undergo scattering processes by emitting phonons due to exciton-phonon or electron-phonon interactions. The formed exciton can relax through phonon emission, eventually recombining the electron with the before left behind hole. This can happen as fluorescence or phosphorescence. Fluorescence refers to an event where the transition from the excited to the ground state happens without changing spin multiplicity, while phosphorescence refers to an event with inter-system-crossing. The relaxation involves a change in spin orientation(see 2.8) [28].

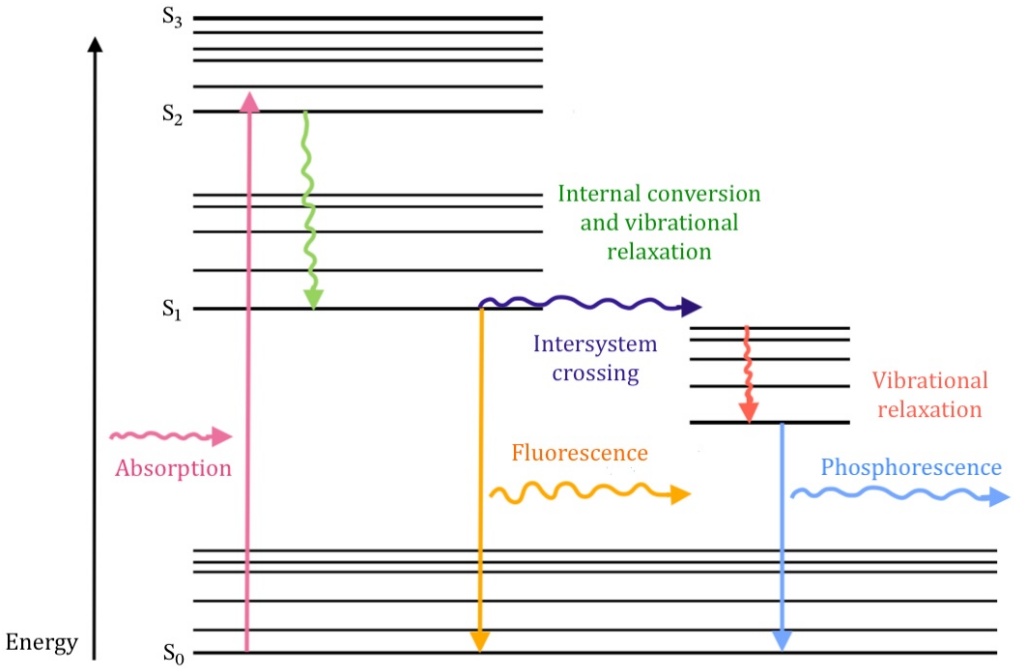

Figure 2.8: Schematic representation of photon absorption and subsequent relaxation processes, illustrating the mechanisms of fluorescence and phosphorescence.

Optical spectroscopy techniques like absorption, photoluminescence, and Raman scattering provide insight into electronic band structure, the vibrational properties, and carrier dynamics of the SWCNTs. Due to the one-dimensional structure of SWCNTs sharp peaks in the absorbance and the photoluminesence spectra are expected whcih correspond to the van Hove singularities in the DOS. Since these optical transitions are unique to each SWCNTs, measuring the optical transitions can be used to find the chirality distribution within the sample[28].

2.3.1 Absorption transition rate and selection rules

An electron within the system can be described by its the quantum number q and momentum k. Therefore, the wavefunction of the electron can be written as $\langle -, q, k|$ for the valence band and $\langle +, q, k|$ for the conducting band [29].
The relationship between an electron and an electromagnetic field can be described using perturbation theory and a semiclassical description of the field. Under the weak field approximation and within the Coulomb gauge, the single-particle Hamiltonian is expressed as[30]:

$$H = H_{el} + H_{em} = H_{el} - \frac{e}{m_e} p \cdot A. \tag{2.36}$$

The process of the excitation of an electron from the valence band to an unoccupied state in the conducting band, can be described by Fermi's golden rule W_{abs}[29]. This rule states the probability of a photon to be absorbed and an electron to excited to the conducting band and is given by[29]:

$$W_{abs} = \sum_{q,q'} \frac{1}{l_{BZ}} \int_{BZ} dk\delta(E^+_{q'}(k') - E^-_q(k) - \hbar\omega) |\langle +, q', k' H_{em} |-, q, k\rangle|^2 f^-_q(k)(1 - f^+_{q'}(k')). \tag{2.37}$$

$f^-_q(k)$ denotes the occupation probability of the initial state and $1 - f^+_{q'}(k')$ of the final state and can be obtained from the Fermi-Dirac distribution[29].
The total absorption rate is determined by the optical transition matrix given by

$$H^{abs}_{qq'}(k, k') = \langle +, q', k'| H_{em} |-, q, k\rangle \tag{2.38}$$

and the joined density of state (JDOS) is given by:

$$J_{q,q'}(\hbar\omega) = \sum_{q,q'} \frac{1}{l_{BZ}} \int_{BZ} dk\delta(E^+_{q'}(k') - E^-_q(k) - \hbar) \tag{2.39}$$

The JDOS describes the permissible optical transitions between the occupied valence band and the unoccupied conduction band, corresponding to a specific photon energy[31] [29].
Since wavelength λ is significantly larger than a_0, the lattice constant, the photon momentum can be neglected[29]. Therefore, following condition can be established for inter-band transitions

$$k' - k = 0. \tag{2.40}$$

Without the momentum dependency the Fermi's Golden rule can be rewriten as [29]

$$W_{abs} = J_{q,q'}(\hbar\omega) |H_{qq'} \hat{a}bs|^2 f^-_q(k)(1 - f^+_{q'}(k')) \tag{2.41}$$

The optical selection determine if a specific transition between two states is optically allowed. These rules are determined by the symmetry of the nanotube and also dependent on the relative polarization of the electric field to the carbon nanotube. Furthermore, since $\Delta k \approx 0$ which means that only vertical transitions are allowed.
Achiral tubes possess a horizontal (σ_h) and a vertical (σ_v) mirror plane. The parity for vectors along the z-axis is $\sigma_h = -1$, while for vectors in the (x, y) plane, it is $\sigma_h = 1$. When a photon is absorbed, then the transition from valence to conducting band must satisfy some rules to ensure the conservation of total angular momentum[4].
For light polarized along the z-axis, the electronic band's angular momentum quantum number m will stay unchanged

$$\Delta m = 0 \qquad for \quad E \parallel z \tag{2.42}$$

while for light polarized perpendicular to z m will change by a either $+1$ or -1[4]:

$$\Delta m = \pm 1 \qquad for \quad E \perp z. \tag{2.43}$$

2.3.2 Raman scattering

Raman scattering was discovered by C. V. Raman and his students and describes the interaction between a photon and matter[32]. This discovery forms the basis for Raman spectroscopy.
Scattering events can be distinguished between Rayleigh scattering and Raman scattering. Rayleigh scattering describes an elastic scattering event, while Raman scattering describes an inelastic process, where the scattered photon is frequency-shifted. In the event of an inelastic scattering event, it can be differentiated between Anti-Stokes scattering, when the photon is shifted to a higher frequency and Stokes scattering if the photon is shifted to a lower frequency. The scattering event describes the interaction between incoming photons and the phonons of the system, during which a phonon can be either created or annhilated. Under the conservation of energy and momentum, the frequency of the incoming photon is ω_i, if the photon is scattered inelastically by a lattice vibration with the frequency ω_{ph}. Then the outgoing photon will have a frequency of $\omega_O = \omega_I \pm \omega_{ph}$[33]. These scattering events are illustrated in Figure 2.11.

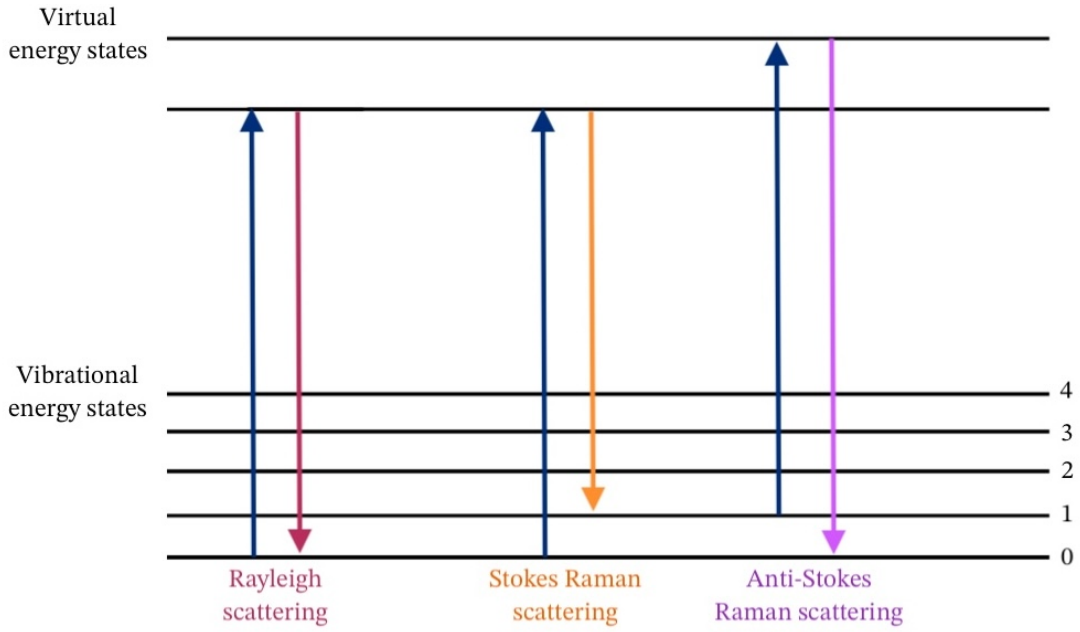

Figure 2.9: Illustration of Rayleigh, Stokes and Anti-Stokes scattering.

Raman spectroscopy is a widely used analytical technique, since it is non-invasive and requires no specific sample preparation. Since the DOS of SWCNTs are governed by van

Hove singularities, a scattering event with an energy close or the same as the energy difference between two van Hove singularities will be enhanced[34]. Therefore, it is a commonly used characterization technique for SWCNTs.

2.3.3 Characteristic Raman modes of CNTs

A general Raman spectra of a SWCNT has peaks from the Radial Breathing Mode (RBM) between $100 - 300cm^{-1}$, which is a feature exclusively observed in SWCNTs, the D-band at $\sim 1350cm^{-1}$ arising from a electron-defect scattering event, the G-mode at around $\sim 1600cm^{-1}$[35], and the 2D-band arising from a second-order Raman scattering process ~ 2680[36].

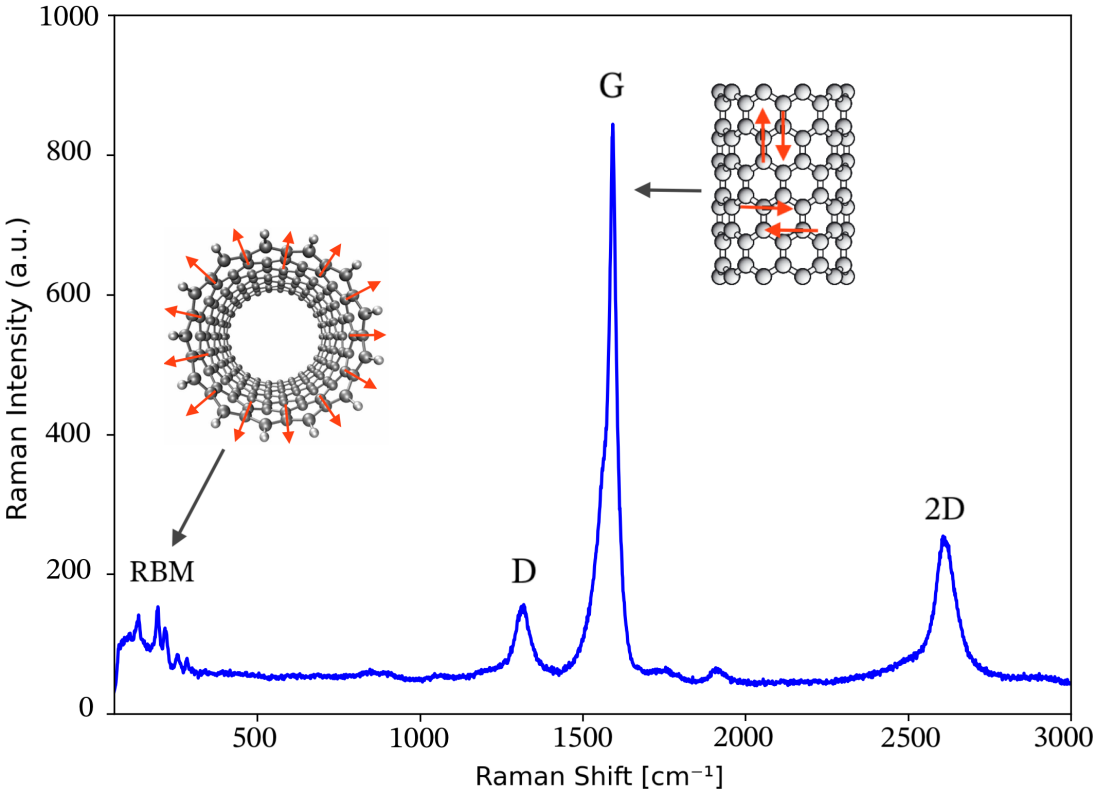

Figure 2.10: Raman spectrum of CBx-SWNTs using a laser of $\lambda = 633nm$ with schematic images or RBM and G-band vibrations. Left inset taken and adapted from [7], Right inset taken and adapted from [8].

Phonon Dispersion

The peaks in a Raman spectra can be assigned to specific phonon branches and atom displacements. The G-band arises from two double degenerate iTO (in-plane transverse optical) and LO (in-plane longitudinal optical) phonons with E_{2g} symmetry at Γ of the

Brillouin zone[9]. The D and 2D band correspond to phonons with A_1' symmetry in the iTO branch [36]. The phonon dispersion can be seen in Figure 2.11

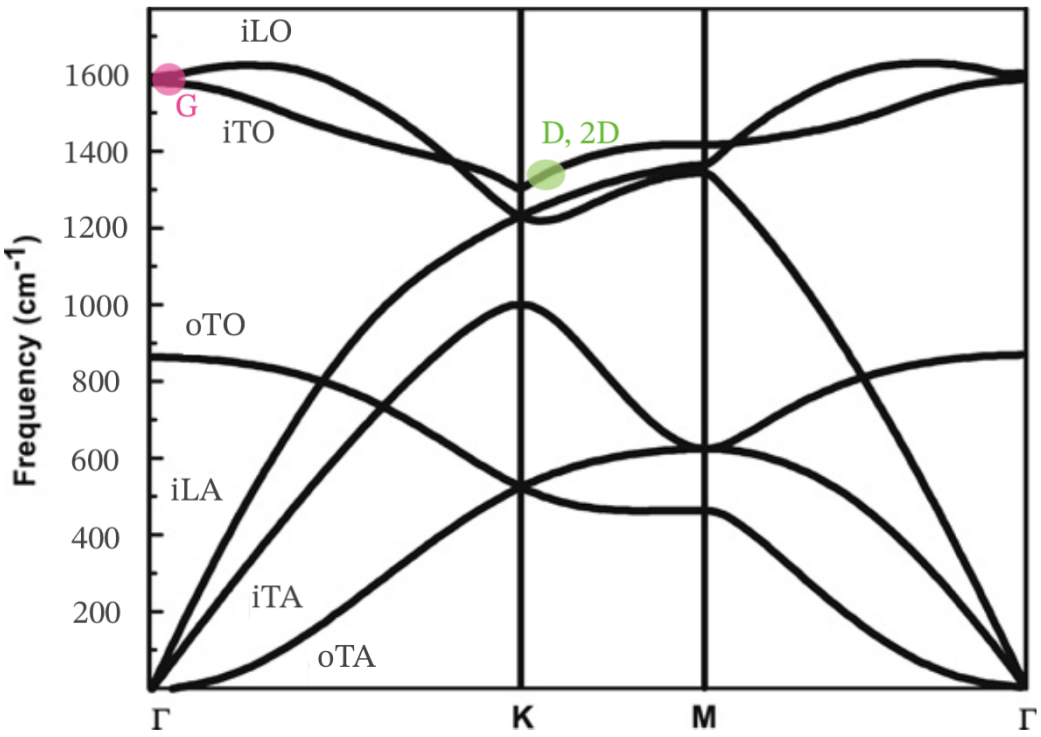

Figure 2.11: Phonon dispersion of graphene. The phonons associated with Raman bands are highlighted. Figure adapted from [9].

G-Band

In the G-band at around $\sim 1580cm^{-1}$, comes from a first-order scattering event from the vibration of the branch between to non-equivalent C atoms in the graphene unit cell. It corresponds to two double degenerate E_{2g} modes for phonons in the iTO and LO branch. Removing this degeneracy, which is the case for SWCNTs, the band splits into two band G^+ and G^- [36]. G^+ being the axial vibrations around $\sim 1591cm^{-1}$ and G^- the circumferential vibration at around $\sim 1550cm^{-1}$ [**?**].

D-band and 2D-band

The D band and 2D-band are the second strongest features after the G-band. The D band is disorder-induced and arises from a defect-assisted one-phonon process and is commonly located at $\sim 1350cm^{-1}$. It is a second order-process involving one phonon in the iTO branch and a defect. The ratio of the intensity of the D-peak to the intensity G-peak provides insight in the amount of disorder present in the sample[37] [36].

The location of the 2D-band is dependent on the excitation frequency of the laser and is located around $\sim 2700cm^{-1}$ for $E_{Laser} = 2.414$[37].

Radial Breathing Mode

The RBM is a distinct characteristic of SWCNTs. Within the tube the atoms vibrate in phase in the radial direction. A nanotube can be approximated by a cylinder, then the frequency of the vibration in the radial direction is given by:

$$\omega_{RBM} = \frac{c_1}{d_t} + c_2 \tag{2.44}$$

d_t the diameter, c_1 a constant and a factor of proportionality of the RMB of a single nanotube and 1/d, c_2, the environmental fitting parameter[38]. This relation allows for the experimental measurement of the tube diameter distribution using Raman scattering. By comparing these experimentally measured diameter values with equation 2.2, the chiral indices can be obtained and the RBM-frequencies can be related to specific (n_1, n_2) nanotubes[39].

2.4 B-doped SWCNTs

The before mentioned properties of SWCNTs open up diverse opportunities for various applications. Tuning the properties of SWCNTs and synthesizing them at high yields is necessary to realize their full potential. This can be done by either introducing a heteroatom into the sp^2 lattice or by adding a functional groups or molecules.
When C is substituted by a heteroatom the chemical, physical and mechanical properties of the structure will change. In semiconductor physics, we can differentiate between n-type and p-type doping. If C is substituted with the heteroatom N, which is in the V group of the periodic table and has one more valence electron than C, it is referred to as n-type doping. However, when C is substituted by an heteroatom B of group III, which has one less valence electron, C can only interact with the three valence electrons of B leaving an electron hole, which is called p-type doping[13] [40].

In this work we will focus on B-doped SWCNTs. Heteroatoms are selected upon their size proximity and their redox behavior upon other parameters. In the table 4.1 the properties of B and C are given

Table 2.1: Details of the electronic structure for B and C[40].

Element	Atomic number (Z)	Electronic configuration	Number of valence electrons	V-d-W radius[pm]	Electronegativity
B	5	$1s^2 2s^2 2p^1$	3	180	$2.04eV$
C	6	$1s^2 2s^2 2p^2$	4	170	$2.55eV$

SWCNTs can exhibit metallic or semiconducting behavior dependent on their geometry, by introducing B into pristine SWCNT structure the electronic properties can be changed with the variation of the dopant concentration. The doped SWCNT can be viewed as structure where some C atoms are replaced by the heteroatoms, therefore, the structures can be compromised depending on the dopant concentration[13].

2.4.1 Properties of B-doped CNTs

Substitutional heteroatom doping, is a technology widely used to change the electronic properties of SWCNTs. To guarantee optimal device performance, the doping levels need to be controllable. Since, the percentage of B in the nanotube will influence the electronic behavior. The substitution of B in the carbon structure forms a triple coordinated bond and creates an electron deficiency, effectively acting as a p-type dopant. This introduces an acceptor state within the band gap and will lower the fermi level towards the valence band[13]. However, B nanomdomains can form during the doping process, where not individual C are substituted by B, but rather islands of dopants form, which also alter the electronic properties[15]. Yi and Bernholc [41] found that for an $(10, 0)$ nanotube and a B concentration of 1.25 at. % an acceptor state at $0.16eV$ above the Fermi energy. In the chapter "Electronic Properties of SWCNTs" the DOS of an undoped SWNT was discussed, which exhibit symmetry around the band gap for both the first and second van Hove singularities. Due to the introduction of B into the system and as a result the overlap of the p- and the s-orbitals asymmetries arise. For the calculation of the DOS the rigid band model was used however, if this is also possible for CBx-SWNTs need to be considered. While for low dopant concentrations, in the range of parts per million, allow the use of the rigid band model, under which the electronic DOS of the doped system is assumed to closely resemble that of an undoped one. With minimal doping, the change of the band structure is negligible, and can be approximated by shifting the Fermi level toward the valence or conduction band. If the doping concentration is higher, then the rigid band model is not applicable anymore, since the changes in the DOS of the dopants need to be taken into consideration[13]. The optical properties of the SWCNTs are governed by the van Hoove singularities, therefore, the introduction of B into the system and the resulting changes of the DOS influences the optical properties of the SWCNTs. The photoluminescence spectra may show variations in peak intensity and position, with possible quenching, due to hole-doping which can lead to an reduction of absorbance and also favors non-radiative recombination[42]. Introducing B into the graphene lattice varies the in-plane and inter-plane atom spacing and therefore, alters the vibrational properties of the system. Raman spectroscopy studies have shown that the D-band intensity increases with dopant concentration and also frequency shifts for the D band, G band have been reported[14]. These spectroscopic changes provide insight into the effects of doping on the electronic, optical, and vibrational properties of SWCNTs.

2.4.2 Sythesis of B-doped SWCNTs

Over the last three decades great progress has been made in the synthesis of carbon nanotubes, however, doped variants, particularly B doped ones, has proven themselves to be a challenge with relatively few studies. Studies on the synthesis of CBx-SWNTs have progressed more slowly compared to multi-walled B doped C nanotubes (CBx-MWCNTs)[43][12]. The first report of successfully synthesizing B and N doped MWCNTs by using a modified arc discharge process was by Stephan et al. ([44]). Currently, CBx-SWNTs are primarly produced using following three synthesis methods: Arc Discharge, Laser Ablation and CVD. Arc discharge synthesizes CNT by the flow of electric current between a high-purity graphite anode and cathode in an inert atmosphere. Stephan et al. [44] used a mixture of graphite powder and B powder $(2:1)$ which was deposited into a hole at the graphite anode to synthesize CBx-CNTs. The arc discharge method offers the benefit of a high nanotube yield; however, arc discharge offers limited control over the nanotube orientation and since catalysts are required, additional purification steps are necessary[45].
The laser ablation method uses a high-power laser to vaporize a B doped graphitic target. A target like this can be prepared by mixing B with catalysts and a carbon paste[**?**]. A variation in diameter can be archived by changes in the furnace temperature, the gas carrier, the flowrate and the laser pulse power. Laser ablation allows the production of CBx-SWNTs under controlled growth conditions and produces at higher quality than arc discharge but also at a higher cost and lower yield. Despite its advantages, this method can result in irregularly grown CNTs with branching, and its scalability is limited[45].
CVD allows SWCNTs to grow aligned and structured on a variety of materials and allows for large scale synthesis. This method uses a catalyst or a catalyst precursor which is prepared on a substrate and placed in a pressure controlled heating chamber. A mixture of hydrogen and hydrocarbons is fed into the chamber, the hydrocarbon molecules are thermally broken down, which causes the carbon atoms to dissolve and accumulate in the metal catalyst. This will eventually lead to the formation of carbon nanotubes as the carbon atoms precipitate off the saturated metal particles. Furthermore, by changing the size of the metal particle it is possible to control the diameter of the CBx-SWNTs[46]. Typical metal catalysts include Ni, Co, Fe, or combinations of these Ni-Y, Fe-Ni, and and the most common carbon sources are methane, acetylene, ethane, ethylene, xylene or a mixture of them[45]. In the case of CBx-SWCNT synthesis with CVD the catalyst/catalyst precursor and a B precursor can be either introduced with the carbon source or already present in the furnace. In literature multiple solid [47], gas [48] and liquid [49] precursors can be found for the synthesis of CBx-Doped SWCNTs by CVD.
Ayala et al. [49] reported the synthesis of B doped SWCNTs by chemical vapor deposition employing high vacuum conditions. A liquid precursor serving as C/B feedstock ($C_9H_{21}BO_3$) and hydrogen gas passes through a horizontal furnace equipped with iron based compounds supported on magnesium oxide. The furnace was kept at optimal temperature of $790-890°C$. The resulting CBx-SWNTs had a narrow diameter range of $0.9-1.5nm$.

Compare to the other synthesis method, CVD has multiple advantages. It enables the growth or aligned SWCNTs at lower temperatures and a high yield can be archived. Furthermore, the diameter and length can be adjusted by modifying the size of the metal particles and the conditions of the deposition environment. Additionally, optimizing the catalytic surface can reduce the amount of unwanted byproduct, which will simplify the purification process[46]. All CBx-SWNTs used in the experiments for this thesis were synthesized via chemical vapor deposition by Carlos Alberto Reinoso Jerez as part of his doctoral research, supervised by Univ. Prof. Paola Ayala at the University of Vienna. As-synthesized SWCNTs exhibit a dopant percentage of $< 0.1\%$ct[49] [50].

3 Materials and Methods

3.1 Materials

The CBx-SWCNTs were synthesized via CVD. A bi-metallic catalyst comprising Fe(NO3)3 20 wt.% supported on MgO powder was placed in a quartz tube furnace under a vacuum of $< 7 \times 10^{-7}$ mbar. After hydrogen reduction from $400°C$ until $\sim 825°C$, triisopropylborate ($C_9H_{21}BO_3$), acting as a precursor and C and B feedstock, was introduced at $16mbar$ for 30 minutes. The as-synthesized doped carbon material mainly consists of CBx-SWNT bundles with few defects and amorphous carbon surrounding them. The material used for all experiments was synthesized and cleaned by Dr. rer. nat. Carlos Alberto Reinoso Jerez during his PhD work as explained in [50] and [51]. The samples have been labeled consistently with the naming conventions used in [51] to maintain continuity. The purification process is described in detail in [51], but I provide a brief overview here. The CBx-SWCNTs were purified in five different ways, four using chemical procedures employing oxidative treatments with different solutions and one using a physical approach. For **PT2** and **P6** hydrochloric acid + peroxide (HCl+H_2O_2) was used while for **PT3** and **PT4** nitric acid 3M (NHO3) was used but at two different temperatures, P3 at 25°C and P4 at 80°C. While for **Pc** DGU was performed.
For the **PT2** purification process 500mg of the as grown material was mixed with a solution of 35ml HCl 37% with H_2O_2 per and magnetic stirred for 12h at room temperature. Then the solution was dispersed in deinoized water, vacuum filtered and then rinsed with deionized water until the pH value reached 7. Then the sample was dried at room temperature for 12h and annealed in air at 450°C for 30min.
For **PT3** 500 mg of material was dispersed in 35ml of HNO_3 and magnetic stirred at 25°C for 12h. Afterwards the same procedure as for PT2 was followed.
For **PT4** the purification is similar to PT3. However, the temperature of the 35ml HNO_3 aqueous solution was kept at 80°C for 12h. Then the same procedure was done as for PT2. The sample **Pc** was purified using a physical approach. The synthesized material was dispersed in DOC 2% (sodium deoxylcholate $C_{24}H_{39}NaO_4$) and tip sonicated with Branson 450 for $4h$. Afterwards the solution was placed in 28ml tubes and ultracentrifuged at 36000RPM (140 000g) for 30 min (120mx Thermo scientific ultracentrifuge with an ST-50 swivel rotor). The supernatant was collected and mixed with acetone and sonicated for 2h. The solution was filtered using Millipore-Type-Jeep-0.2nm. The filtered solution was dispersed again and sonicated for 20 min. Then the solution was filtered again and dispersed with methanol and sonicated for 20 min. Afterwards, the solution was filtered a third time and rinsed again using hot water at $70°C$. This procedure was done four times, subsequently the specimen was dried at room temperature. The purification process of

P6 follows following steps: the sample was dissolved in H_2O_2 30% and sonicated for 1h, then washed with water and disolved in HCl 37% and sonicated for $30min$ then washed with water and filtered using Millipore-Type-Jeep-$0.2nm$ and then dried. The dried material was annealed in air for 1h at 350°C. Afterwards the material was dispersed in a $1.5\%DOC$ and $1.5\%SDS$ $(CH_3(CH_2)_{11}C_6H_4SO_3Na)$ solution and ultracentrifuged at $50000RPMs$ for 2h. The supernatant was collected and washed in a milipore for several times. After the purification process chirality sorting was attempted using DGU. The workflow of the experiment is illustrated in 3.1.

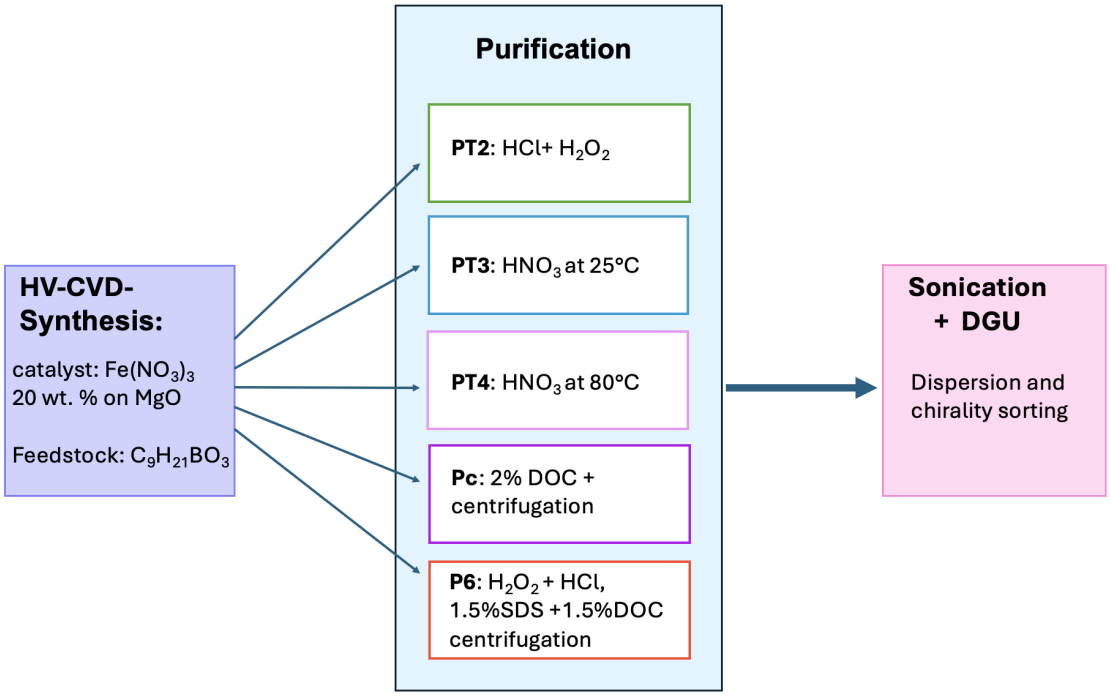

Figure 3.1: Schematic representation of the experimental workflow, illustrating the different steps. The as synthesized material was purified using 5 different purification pathways (PT2, PT3, PT4, Pc, P6) followed by the sorting process via DGU.

3.2 Density Gradient Ultracentrifuge

DGU is a technique used to purify the synthesized samples, and has also been employed for the possibility of sorting CBx-SWNTs by chirality. While amorphous carbon, is relatively easy to oxidize and remove under mild conditions, removing graphitic and polyhedral carbon particles is more tricky, due to similar oxidation degree as the SWCNTs. Metal catalyst particles are often encapsulated within nanotubes or coated by carbon layers which makes it harder to remove them with acid[18]. However, DGU can effectively

remove graphitic impurities, bundled SWCNTs, graphite, and amorphous carbon.[52].
DGU separation and purification is done by creating a density gradient within a centrifuge tube with different surfactants. Due to the strong centrifugation, SWCNTs species will settle in the layer corresponding to their buoyant density. Dense parts will fall to the bottom of the tube[20]. The sample material was dispersed in a 2% DOC solution and put into a sonication bath for $6h$, afterwards the sample was tip sonicated at $30Hz$ for $30min$.
Then the solution was put into centrifuge tube and centrifuged at $38000rpm$ $(146000g)$ for $30min$, allowing large aggregates and impurities to settle at the bottom of the centrifuge tube. Then the supernatant, which remains at the top was carefully collected (around 90% of the solution). For the next step a density gradient, using iodixanol (IO $C_{35}H_{44}I_6N_6O_{15}$) was created within the centrifuge tube, as shown in 3.2, for the sorting and purification of the CBx-SWNTs.

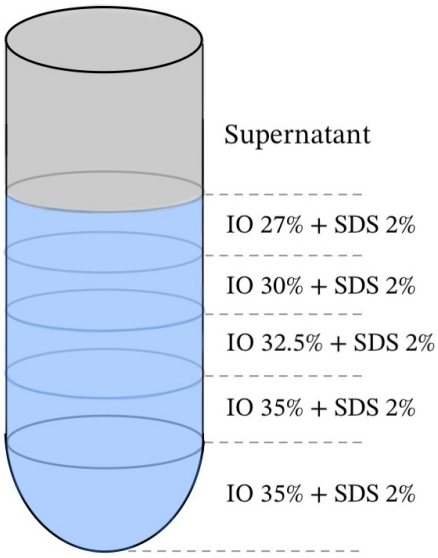

Figure 3.2: Illustration of of the density-gradient layers in the centrifuge tube, with the supernatant at the top.

From the bottom to the top the solutions are IO 40% and SDS 2%, IO 35% and SDS 2%, IO 32.5% and SDS 2%, IO 30% and SDS 2%, IO 27% and SDS 2% and then the supernatant, which was collected in the previous step. The tube with the density gradient was centrifuged at $42000rpm(178000g)$ for $10h$, then the sample should prefferable be separated in multiple layers.
All layers were analyzed using optical absorption spectroscopy to evaluate the effectiveness of the filtering process. Layers exhibiting well-defined absorption spectra were measured with photoluminescence (PL) spectroscopy. This technique was employed to generate PL maps, enabling the identification of specific CBx-SWNT species present in the samples.

3.3 Optical techniques

Optical spectroscopy techniques, such as absorption, photoluminescence, and Raman spectroscopy, provide insights into the physical properties of systems. The spectra of SWCNTs arise from their 1D nature and is governed by van Hove singularities, though these features become only apparent when the tubes are isolated. Absorbance and photoluminescence processes differ primarily in their timescales and mechanisms, with Raman scattering offering detailed information about vibrational and electron-phonon interactions.

3.3.1 Optical Absorption Spectroscopy

Optical absorption spectroscopy is a technique, which probes optical transitions, by directly exciting an electron from the valence to the conduction band.
It can be used to asses the SWCNT concentration and the purity of the sample, before further investigations. The intensity of the absorption is proportional to amount SWCNTs present in the sample and the peaks correspond to the optical transition energies E_{ii} between the van Hove singularities. These resonant peaks in the absorbance spectra can therefore be assigned to specific chirality species. As electromagnetic radiation travels through an absorbing medium like, its intensity diminishes according to the extinction coefficient (ϵ), the optical path length (l), and the concentration (C) of the material present[53]. Optical absorption spectroscopy measures the attenuation of the radiation as function of the frequency or wavelength. The decrease of the intensity is described by the Beer - Lambert law

$$A = log_{10}(\frac{I_0}{I}) = \epsilon C l \tag{3.1}$$

where the ratio is sometimes summarized as a transmittance coefficient $T = \frac{I}{I_0}$ [53].
The peaks in an optical absorption spectra arise from the symmetric inter band transition between the $i-$th valence and the conducting band denoted by E_{ii}[54] [13]. The optical absorption spectroscopy data presented in this work was obtained using a Bruker VERTEX 70v/80v FT-IR Spektrometer. It is a Fourier transform infrared spectroscopy (FTIR) spectrometer which uses a Michelson interferometer, with a broadband infrared source, a beam splitter, a fixed and a movable mirror. The sample is placed between between the beam splitter and the detector. FTIR allows to scan over different optical path length differences by adjusting the distance between the beam splitter and the moving mirror. The intensity $I(\delta)$ for each path length difference δ is measured and the spectrum is determined by computing the Fourier transformation $F\{I(\delta) - I(0)/2\}$[55].
In this thesis, optical absorption was employed to characterize the different layers after attempting sorting with DGU. This technique was used to investigate the different layers and differentiate between the layers with clear absorbance peaks and the layers with impurities such as amorphous carbon. The absence of the characteristic absorbance peaks suggests that this layer is likely composed predominantly of impurities.

3.3.2 Photoluminesence Spectroscopy

If an electron is excited to a higher energy band a positively charged vacancy or "hole" is left. The hole and the photo-excited electron can interact with each other via Coulomb interactions and form en exciton. When the exciton relaxes it emits a photon, this phenomenon is known as photoluminescence[56].
The experiments were conducted with the photoluminesence spectrometer Fluorolog from Horiba, it uses diffraction gratings, and therefore no FTIR has to be performed. After calibration, the sample is inserted and the excitation swept over a range of wavelengths in 5nm increments and the emission spectra was recorded. Since each nanotube has a unique combination of the absorbance photon E_{22} and the emission photon E_{11} a Photoluminesence map can be created from the measurement. This map can the be used to identify the nanotubes present in the sample.

3.3.3 Raman Spectroscopy

The Raman spectroscope Horiba LabRAM HR800 was used. The system is equipped with a He-Ne laser operating at $\sim$ $633nm$. Raman shifts are recorded using a liquid nitrogen-cooled CCD detector in combination with a $50x$ objective (numerical aperture: 0.5), a $1000\mu m$ pinhole, a $100\mu m$ slit, an 800 mm confocal length, and a 600 Gr/mm grating. The sample is placed in aluminium foil, since it provides almost featureless background signal and enables the acquisition of Raman spectra without substrate interference. Then the sample was placed inside the optical window, a movable lens is used to position a camera in the path of the back scattered light, ensuring optimal focus of the incident laser beam on the sample. "A He-Ne laser was used as source and directed through the spectrometer and a series of optical filters to minimize background noise. The beam was then focused onto the sample using a 50x objective lens. Backscattered light from the sample was collected and detected by a CCD detector. Raman measurements were performed in acquisition windows of 30 seconds, with five scans per window, and the resulting spectrum was automatically combined to generate the final signal.

4 Optical spectroscopy Results

4.1 Overall morphology

The spectra shown here were recorded using the JY-Horiba HR800 Spectrometer with a He-Ne laser operating at 633nm. I did not perform a multi-frequency Ramen analysis. The diameter overview of my samples was done via OAS. Raman was used to understand the quality of the material. The measurements were conducted in windows with an acquisition time of 30 seconds. Figure 4.1(a) shows the spectra recorded in the radial breathing mode (RBM) region, while Figure 4.1(b) displays the spectra in the D, G, and 2D regions. The vertical lines indicate the peak positions for the as-grown materials. The corresponding values were taken from [51]. In the as-grown material, the carbon sp^2 hybridized state shows the G peak at 1588 cm^{-1}, the D band at 1318 cm^{-1}, and the 2D peak at 2600 cm^{-1}[51]. The investigated samples PT4 and PT3 were purified using nitric acid at two different temperatures PT4 at 80°C and PT3 at 25°C. Then washed until pH=7 and annealed in air at 450°. The sample PT2 was purified using a mix of 35ml HCl 37% with H_2O_2, the solution was magnetic stirred then the same steps followed as for PT3 and PT4. The sample Pc was purified using DGU, the sample was dispersed in DOC 2% and tip sonicated for 4h. After dispersion the sample was centrifuged for 30min at 36000RPM (140 000g), followed by multiple washing and filtering steps and then dreid ar room temperature. P6 was purified using H_2O_2 30% and HCl 37% consecutively, then washed, filtered and annealed at 350° followed by dispersion in 1.5% DOC and 1.5%SDS and centrifuged at 50000RPMs for 2h. The supernatant was collected. In comparison to the as-grown material, the results for G-band of the purified CBx-SWCNTs show a slight shift to higher frequencies except for Pc where there is no shift observed. The tangential G-mode does not exhibit a clear separation between the G^- and G^+ components. The G^- component appears most prominent in PT4, with some enhancements also observed in Pc and P6. This could be attributed to the presence of small-diameter nanotubes and contributions from metallic species[21].
For P3 and P4 the G-band is upshifted to 1592nm−1 and 1593cm−1, respectively, this could be due to charge transfer from the nanotube bundle to form an NO_3^{-1} anion[57]. While the D-band is slightly upshifted, 6cm−1 and 4cm−1, for P3 and P4 respectively. One possible explanation is that the acid treatment introduces defects, which weaken the carbon network and reduce the vibrational energy. The sample Pc shows no shifts in the D-band and only a slight shift in the G-band $\sim 4cm^{-1}$, suggesting that the purification process had little effect on the vibrational modes of the material. The sample P6 shows a slight shift in the D band $\sim 5cm^{-1}$ and G band $\sim 4cm^{-1}$. The D-band is related to defects within the sample and provides insight into the degree of disorder in the hexagonal

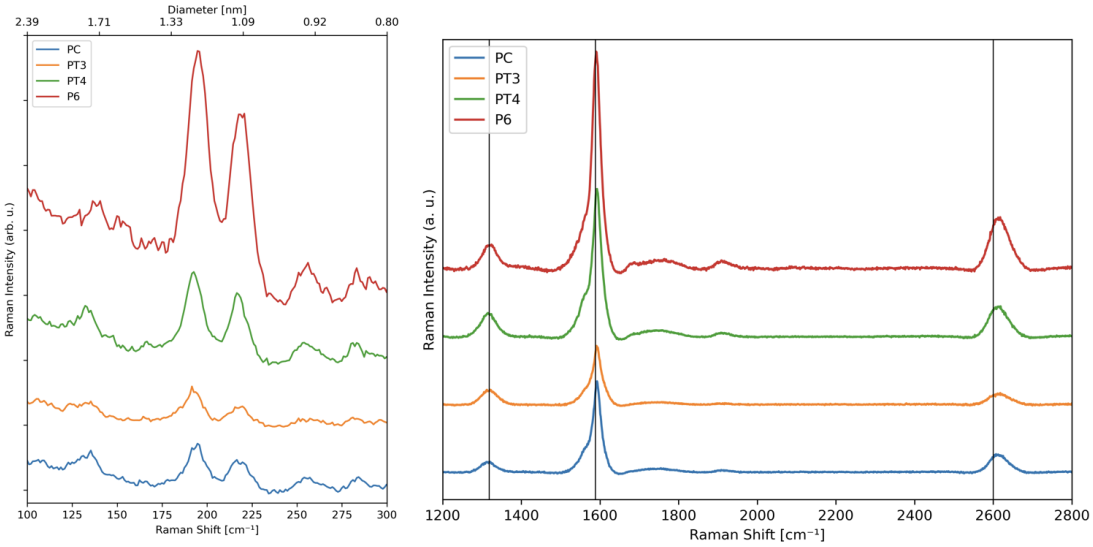

Figure 4.1: Raman spectra of boron-doped SWCNT samples. (a) Spectra in the RBM region; (b) Spectra in the D, G, and 2D regions.

lattice. It is well established that the introduction of B into the graphene lattice leads to an increase in disorder [14]. However, a strong D-band feature could also stem from impurities that could not be removed during purification, or from defects introduced during the purification process itself. The $\frac{I_D}{I_G}$ ratio was calculated for each sample and is presented in Table 4.1. This ratio is used as an indicator of the relative defect content within a sample.

Sample	I_D/I_G
Pc	0.17
PT3	0.36
PT4	0.22
P6	0.26

Table 4.1: Calculated $\frac{I_D}{I_G}$ ratios for boron-doped SWCNT samples after different purification methods.

The lowest relative defect content was found for the sample Pc which was purified using DGU suggesting that this physical purification method is effectively maintaining nanotube quality, while removing impurities. The sample P6, was treated with H_2O_2 and HCl subsequently for 1h and 30 min, respectively, followed by dispersion in 1.5% SDS and 1.5% DOC and a centrifugation step. H_2O_2 and HCl are less aggressive than HNO_3, which was used for PT3 and PT4. The relatively high defect index observed for sample P6 compared to Pc, may be attributed to oxidative damage from the acids, which could have introduces functional groups and defects leading to a higher relative defect index

compared to Pc. The highest defect ratio, was found for PT3. This sample was purified using HNO_3 at 25°C for 12h. This method can introduce a significant number of oxygen containing functional groups and defects. The sample was annealed in air at 450°C for 30min to remove some of the oxygen groups, however the annealing time and temperature can also promote the creation of defects. PT4 was purified the same way as PT3 with a small difference, the sample was magnetically stirred with HNO_3 at 80°C instead of 25°C. The higher temperature should introduce a greater amount of oxidative damage to the nanotube structure and therefore increasing the relative defect content. However, the results show that this was not the case. Although HNO_3 at 80°C is more aggressive than at 25°C it might have introduces less stable defects which are more easily removed during the annealing process, resulting in fewer defects overall. The sample PT2 was not measured using Raman spectroscopy, since after the measurements of OA and PL no sample remained. Carlos [51] reported, in his thesis a defect index of $\frac{I_D}{I_G} = 0.21$ for PT2, indicating low damage. However, the specific wavelength used for this Raman measurement is not disclosed, therefore a direct comparison is not possible.
The radial breathing modes (RBMs) are related to the nanotube diameter through the equation $d = \frac{239}{\omega_{RBM}}$ [58], and the diameters where calculated. However, to measure the complete diameter distribution multifrequency Raman spectroscopy has to be done. This technique uses multiple laser wavelengths to resonate with a wider range of electronic transitions, enabling a more comprehensive characterization of SWCNTs and the detection of RBMs corresponding to various chiralities. However, multifrequency Raman spectroscopy was not conducted as part of this Master's thesis.

4.2 Diameter distribution of CBx-SWCNT in OA

Since DGU separation relies on surfactants organizing around CBx-SWNTs, influencing their dispersion in water and medium density, the nanotubes should settle at the layer corresponding to their density[20]. The DGU process is detailed in the chapter titled "Sample Preparation". The layers were extracted after the DGU process and the optical absorbance was measured of each layer. The absorption measurements were performed by recording the spectrum of the extracted layer and the spectrum of the corresponding solution without nanotubes. The reference spectrum was subtracted from the spectrum of the layer, the reference solution providing a baseline absorbance value. Although baseline/solvent background correction were performed, the absorbance spectra exhibit a gradual upward rise at higher energies. This effect is attributed to residual light scattering within the sample, which becomes more pronounced at higher energies. Despite this background trend, the characteristic absorption peaks remain clearly distinguishable In figure 4.2 the optical absorption spectra can be seen. The layers PT2.2 to PT2.5 exhibit well-defined absorption peaks, which correspond to the first E_{11} and second E_{22} transition between the valence and conduction band. PT2.1 does not exhibit distinct absorption peaks, indicating the absence of well-defined chiral species within this layer. This means that after the DGU process most chirality species settled in the layers two to five.

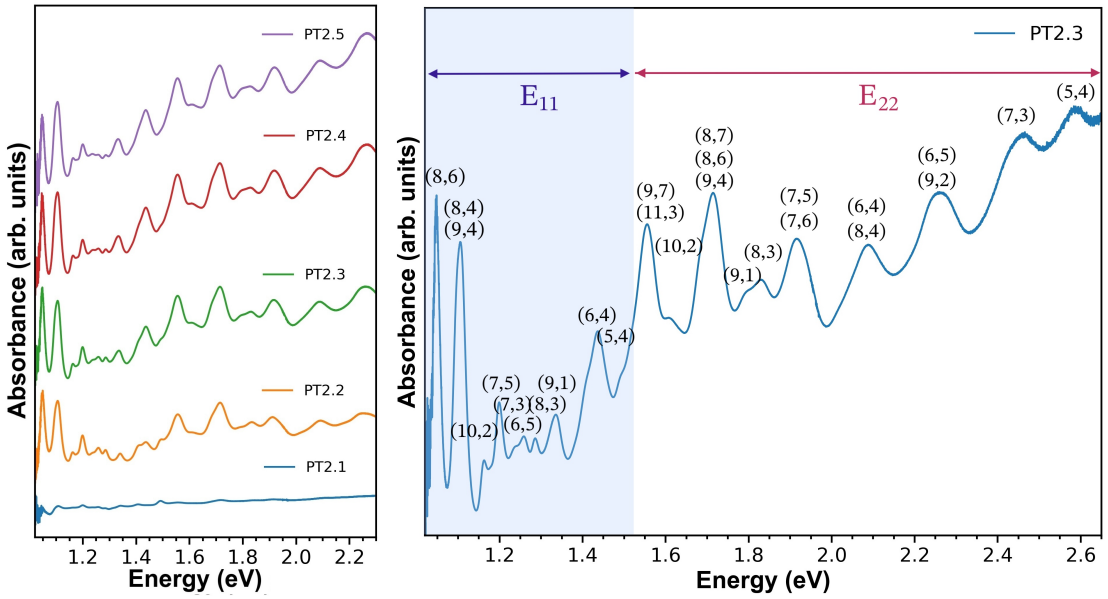

Figure 4.2: Left Figure shows the Optical absorption spectra of PT2. Right Figure displays the optical absorption spectrum of the layer PT2.3 with the chiralities assigned to their corresponding peaks.

The absorption spectrum of the third layer of PT2 is displayed in the right Figure in 4.2, and the first and second optical transitions E_{11}^S and E_{22}^S of the CBx-SWCNT chiralities have been identified using the experimental data from Weisman and Bachilo [59]. This sample was purified using HCl and H_2O_2 stirred for 12h, rinsed and subsequently annealed at 450°C. The mild acid treatment successfully eliminated catalyst residues and amorphous carbon, while maintaining the integrity of the CBx-SWCNT structure, including that of tubes with small diameters.
The left Figure in 4.3 the optical absorbance of the three extracted layers of the sample PT3 can be seen. For this sample only 3 layers could be extracted which could be measured with optical absorption spectroscopy, due to high optical density in the other sample, which is likely caused by a high concentration of aggregates which impeded light transmission. Only one layer PT3.3 displays distinguished absorption peaks. Due to the acid treatment of PT3 during the purification step, oxidation can occur. This could also explain the absence of absorbance peaks in the layers PT3.1 and PT3.2. While the HNO_3 treatment improves purity it can introduce defects due to nitric acid being of stronger oxidative nature than HCl or H_2O_2, which was used in PT2. This can lead to increased quenching of certain transitions [18]. In the right Figure in 4.3 the optical absorbance of the layer PT3.3 with the assigned chiralities can be seen. Similar to PT2, PT3 exhibits a wide range of chiralities with the smallest diameter of $\sim$ 0.7nm for (7,3) and the largest diameter of the chirality (9,7) of $\sim$ 1.1nm.

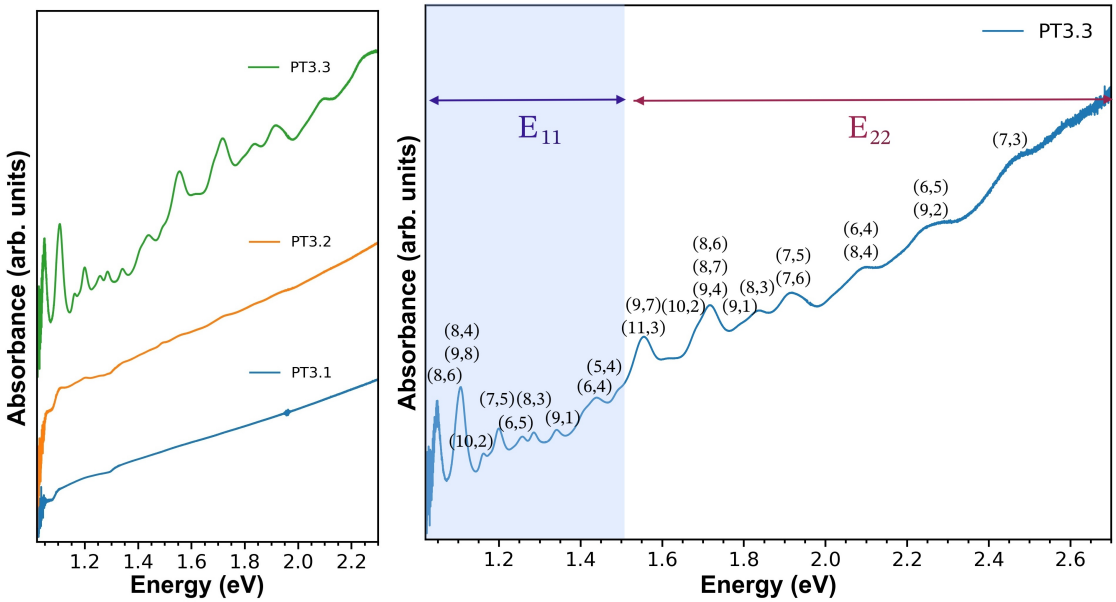

Figure 4.3: Left Figure shows the optical absorption spectra of PT3. Right Figure displays the optical absorption spectrum of the layer PT3.3 with the chiralities assigned to their corresponding peaks.

The left Figure in 4.4 shows the optical absorbance of the layers extracted after DGU from the sample PT4. It shows the same absorbance peaks as PT3, however the peaks are more refined. PT4 followed the purification process similar to PT3 but with an elevated temperature of $80°C$ during acid treatment. The elevated temperature facilitates the more efficient removal of amorphous carbon, thereby contributing to the purity of the sample. When comparing PT3 with PT4, it is evident that the absorbance peaks of PT4 are slightly more defined. Additionally, the absorbance corresponding to (5,4) is also observable in PT4 but not in PT3. The left Figure 4.5 shows the optical absorbance spectrum of all the layers analyzed in sample Pc, while on the right the optical absorption of the layer Pc.2 is depicted with the assigned chilarilties. However, comparing these two it can be seen that the peaks of PT2 4.2 are sharp peaks, while for Pc the peaks are broadened or less resolve. This difference may be attributed to several factors, such as stronger bundling of the tubes, a larger diameter diversity, or the effects of doping or defect creation. Unlike the other samples which were acid-treated, Pc shows lower absorbance peak intensity across and less defined peaks the observed. The centrifugation and the subsequent filtration steps may have resulted in a lower overall CBx-SWNT yield.
The lfet Figure in 4.6 shows the optical absorption spectra of the layers P6.1 to P6.7 which also exhibit distinct peaks associated with the optical transitions of the CBx-SWNTs present in the sample. The layers P6.8 to P6.11 do not display any significant

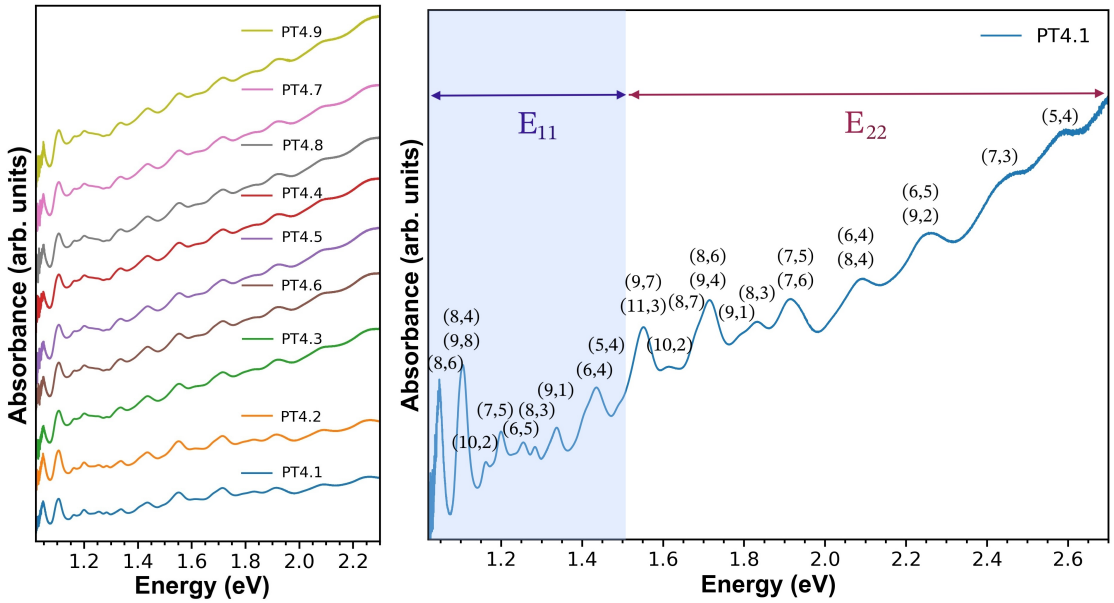

Figure 4.4: Left Figure shows the Optical absorption spectra of PT4. Right Figure displays the optical absorption spectrum of the layer PT4.1 with the chiralities assigned to their corresponding peaks.

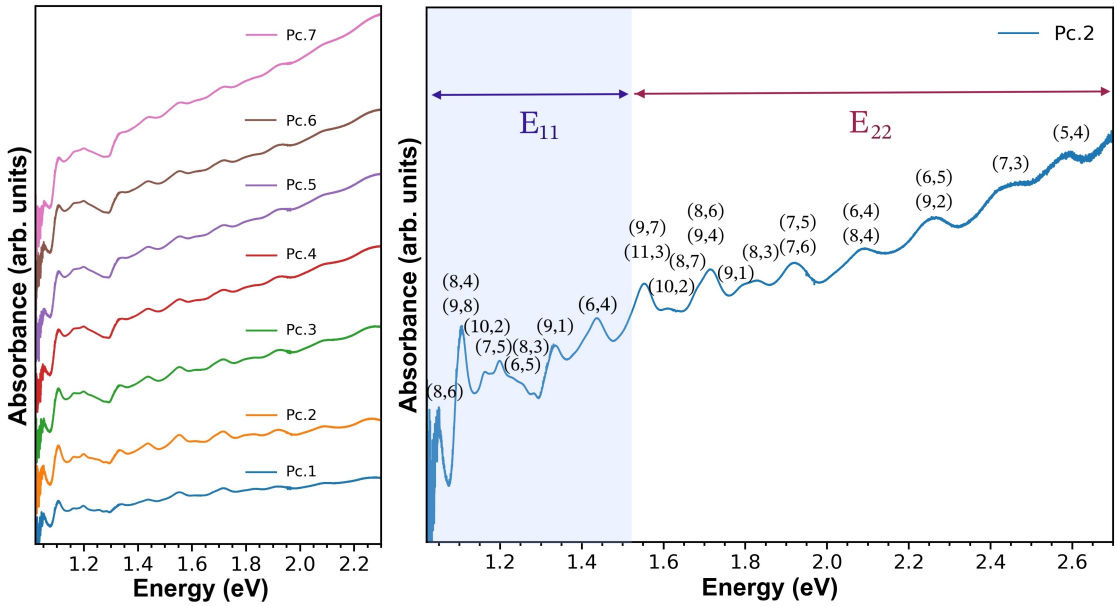

Figure 4.5: Left Figure shows the optical absorption spectra of Pc. Right Figure displays the optical absorption spectrum of the layer Pc.2 with the chiralities assigned to their corresponding peaks.

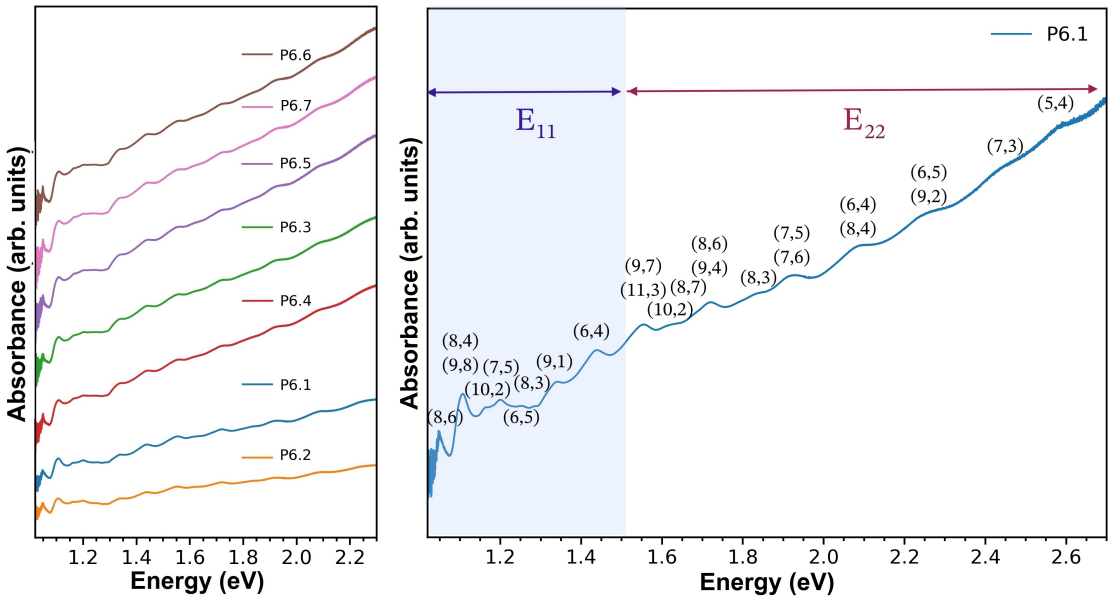

Figure 4.6: Left Figure shows the optical absorption spectra of P6. Right Figure displays the optical absorption spectrum of the layer PT6.1 with the chiralities assigned to their corresponding peaks.

peaks, indicating the absence of CBx-SWCNTs or the possibility that factors such as poor dispersion or bundling may have suppressed their optical transitions. The smallest diameter observed in this sample is (6,4). The method used to purify P6 involved oxidation with H_2O_2 followed by sequential treatment with HCl, and annealing at 350°C, and a centrifugation step. The final step might have resulted in material loss, potentially accounting for the reduced absorbance intensities.
The optical absorbance spectra were measured to investigate the influence of the different cleaning procedures on the resulting material. Some transition energies E_{ii} of different chiralities lie very close, making it challenging to resolve their individual contributions in the spectrum. This highlights the difficulty in distinguishing between nanotubes with different chiral indices but similar E_{ii} optical transition energies. Some layers exhibited strong absorbance peaks, indicating a higher concentration of SWCNTs, as well as less bundling, while others exhibited weaker peaks or negligible absorbance. These observations are critical for assessing the efficiency of the separation and the quality of the purification process. The results presented indicate that sample PT2, which underwent purification via mild acid treatment, effectively removed residues from catalysts and amorphous carbon, while preserving the CBx-SWCNT structure, including small diameter tubes such as (5,4) and (6,4). The samples PT3 and PT4 have been purified using a stronger acid treatment with HNO_3 which can lead to introduced defects due to oxidation and increase quenching of certain transitions. While, similar to PT2, PT3 exhibits a

wide range of chiralities, the peaks appear broader and less distinct than in the other optical absorption spectra. PT4 was purified using the same pathway as PT3, however the acid treatment was done at 80°C instead of 25°C. An increase in temperature aids in the more effective elimination of amorphous carbon, thus enhancing the sample's purity. Comparing PT3 to PT4, the absorption spectra show slightly sharper peaks. Additionally, the absorbance associated with (5,4) is visible in PT4. The sample P6 was purifies using oxidation with H_2O_2 followed by sequential treatment with HCl, then the sample was annealed at 350°C, and centrifuged. The centrifugation step might have resulted in material loss, which would explain the reduced absorbance intensities but could also be from induced defect due to the acid treatment. The sample Pc which was purified using a soley a physical approach shows lower absorbance peak intensity across the observed chiralities compared to PT2, PT3 and PT4. The reason for this could be that the sample contains less well-dispersed CNx-SWNTs, which may lead to lower absorption. It could also be that the DGU purification lead to a loss of some chirality species. Due to the presence of multiple chiralities some absorption features appear broadened, especially in regions where transitions from different chiralities closely overlap as is the case for (8,6), (9,4) and (8,7). Therefore, photoluminesence was measured to confirm the species present within the sample.

4.3 Effect of purification methods on the PL

The data obtained from optical absorption spectroscopy was analyzed to identify the presence of characteristic peaks and implicitly, the chiralities. Based on that, the range of the corresponding excitation wavelengths were selected. The chosen sample was measured with the photoluminescence spectrometer Fluorolog from Horiba. After calibration, the sample was inserted and the excitation swept over the preset wavelength range in steps of 5nm, and the emission spectrum was recorded.
The data from the photoluminescence measurements consist of three key parameters: excitation wavelength, emission wavelength, and intensity. From this 3D model (see Figure 4.7) a 2D photoluminescence (PL) map can be constructed by plotting the intensity as a function of both excitation and emission wavelengths. This map allows for the identification of the specific chiralities of single-walled carbon nanotubes present in the sample.

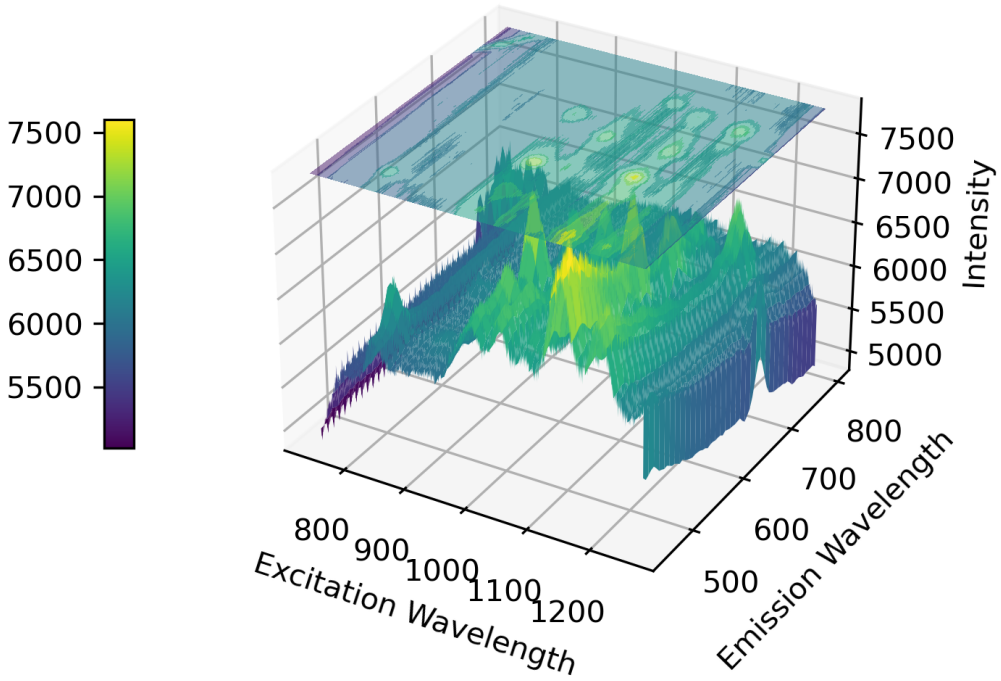

Figure 4.7: 3D-photoluminesence spectra of PT2.2 with the corresponding PL map.

PL spectroscopy requires a specific sample volume for measurement. However, due to variations in the amount of liquid of different layers after the DGU process, some did not have a large enough volume to measure PL. Consequently, a layer exhibiting well-defined peaks and an adequate sample volume was selected for subsequent measurements.
The peaks of the PL map were identified using the experimental data from Weisman and Bachilo [59]. The PL map of the third layer of PT2 can be seen in 4.8a, it shows a broad range of chiralities. The chirality distribution can be seen in 4.8b, the highest intensities

are observed for (8,4), followed by (6,5) the weakest signals appear for (5,4), (6,4). The (5,4) chirality is close to the boundary of robustness, due to curvature effects [60]. The low signal for (5,4) and (6,4) could also be related to the oxidization of the tubes by O_2 since literature showed preferential oxidization of small diameter SWCNTs [61]. (5,4) is the smallest diameter ($\sim 0.62nm$) tube that could be found. The application of mild acid treatment proved effective in eliminating catalyst residues and amorphous carbon, while successfully maintaining the integrity of the CBx-SWCNT structure, including tubes of small diameters.
In Figure 4.8c the PL map of the sample PT3.3 can be seen. Due to the acid treatment during the purification step, oxidation can occur, which may explain why PT3.1 and PT3.2 consist of highly oxidized, defective, or amorphous carbon-rich fractions. While the HNO_3 treatment improves purity, it may have also introduce functional groups due to oxidation[18]. Similar to PT2, PT3 exhibits a wide range of chiralities, with strong PL intensities.
In Figure 4.8d shows the chiralities present in the sample versus the measured intensity. Figure 4.8e shows the PL map of PT4.1 and 4.8f shows the chirality distribution within the layer. PT4 follows a similar purification process as PT3 but with an elevated temperature of 80°C during acid treatment. The increased temperature enhances the removal of amorphous carbon which should lead to a purer sample [18]. While PT4 shows strong signals for (8,4), (8,6) and (6,5), it also shows that signal losses for other chiralities. The more aggressive oxidation conditions could have introduced a higher number of defects, which can explain the overall lower signal compared to PT3 where the acid treatment was done at 25°C. The elevated temperature during this step, leads to stronger oxidization since HNO_3 acts more aggressively. These introduced defects, increase the non-radiative recombination and therefore can reduce the fluorescence signal. Figure 4.8f shows the chiralities within the sample versus the PL intensity. High PL intensities can be seen for the chiralities (6,5), (8,4) and (8,6) as it was for PT3 and PT2. This could be an indicator that either these chiralitities are abundant in the starting material or that this DGU protocol preferentially selects these chiralities. The 2D contour plot for Pc2 can be seen in Figure 4.8g and in Figure 4.8h the chirality species of the layer Pc2 can be seen. Unlike the acid-treated samples, Pc shows significantly lower PL intensity across all observed chiralities. The centrifugation method may have resulted in a lower overall yield. Furthermore, the multiple filtration and drying steps could have led to material loss. Additionally, prolonged sonication during purification may have introduced defects, increasing non radiative recombination and reducing the photoluminesence signal.

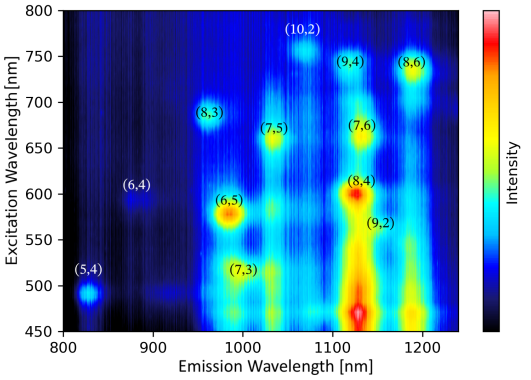

(a) PL map of PT2.3 layer

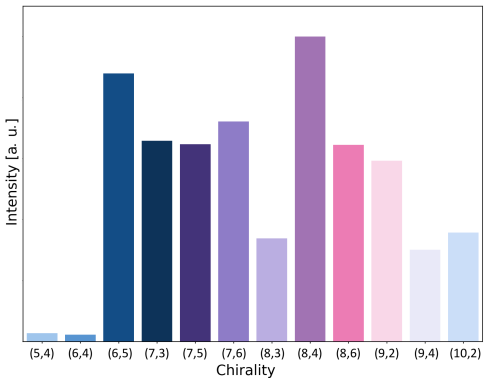

(b) Chirality distribution of PT2.3

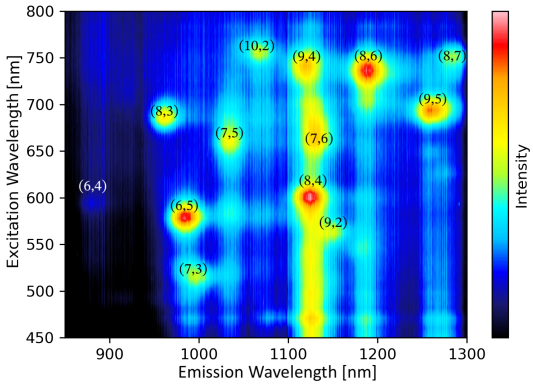

(c) PL map of PT3.3 layer

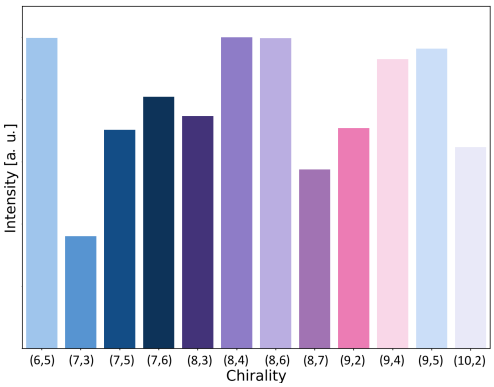

(d) Chirality distribution of PT3.3

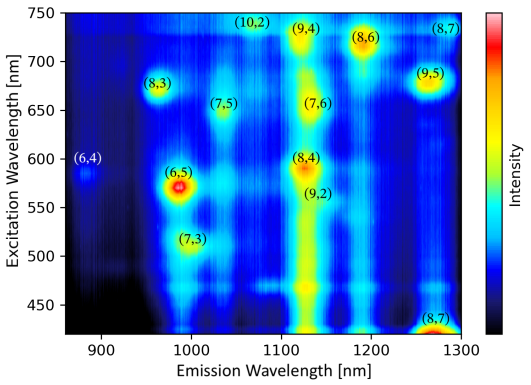

(e) PL map of PT4.1 layer

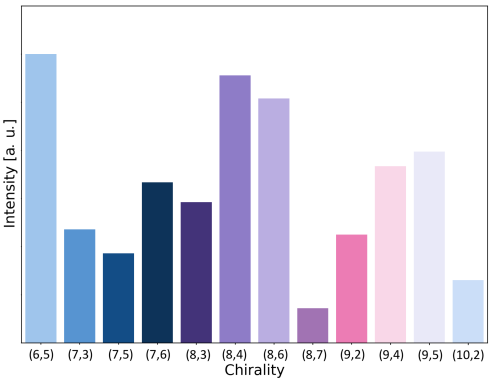

(f) Chirality distribution of PT4.1

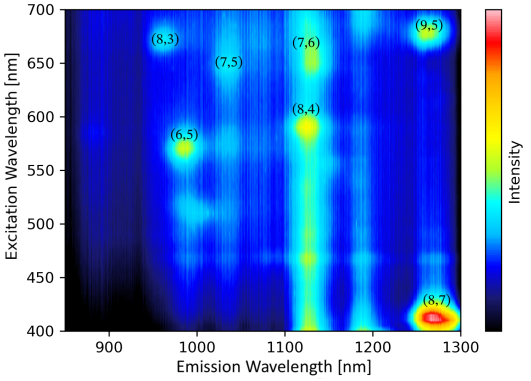

(g) PL map of Pc.2 layer

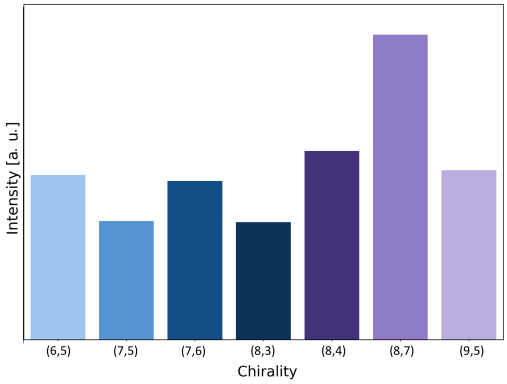

(h) Chirality distribution of Pc.2

Figure 4.8: Comparison of PL maps and corresponding chirality distributions for the layers PT2.3, PT3.3, PT4.1, and Pc.2.

The PL map for sample P6 can be seen in Figure 4.9, it displays a much more selective PL response, with strong signals only for (6,5) and (8,3). The purification method involved oxidation with H_2O_2, which can introduce oxygen functional groups and can lead to PL quenching. However, the sequential treatment of HCl and annealing at 350°C likely helped to remove some defects, preserving emission from select chiralities. The sorting via DGU may have further sorted the SWCNTs, favoring the enrichment of (6,5) and (8,3). For this sample the chirality seperation with DGU was very effective. The high PL intensities of these chiralities suggests that this process effectively isolated these specific semiconducting chiralities while removing others.

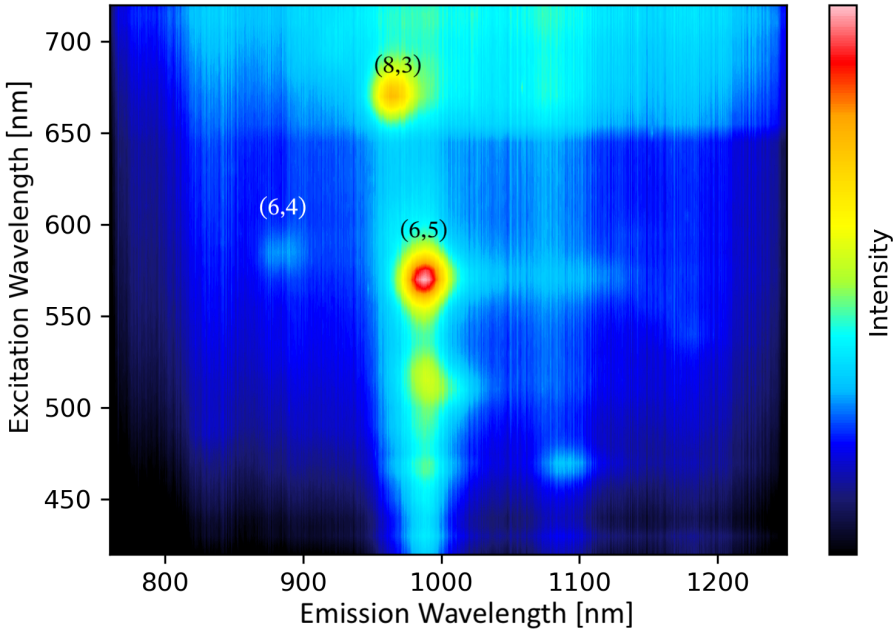

Figure 4.9: PL map of the P6.1 layer.

When comparing the five purification methods with the subsequent sorting, we can see that PT2, PT3, and PT4 are all effective purification protocols for achieving a high yield of a wide variety of CBx-SWCNT chiralities. Specifically, PT2, which employed mild hydrochloric acid, was the only purification method preserving small diameter tubes such as (5,4). On the other hand, the purification approach Pc is less effective. One reason for this could be that the samples treated with acid dispersed better and therefore made the sorting process more efficient. Out of the five samples purified via different pathways and subsequently sorting, one resulted in the isolation of mainly two chiralities. This outcome may be attributed to the specific purification conditions, which could have selectively damaged or removed other chiralities, or affected the surfactant coverage and dispersion quality needed for effective separation. Although isolating a single chirality was not achieved, the purification pathway P6 and sorting by DGU successfully isolated the (6,5) and (8,4).

5 Conclusion and Outlook

This work focused on the characterization CBx-SWCNTs, heteronanotubes, which compared to pure C-SWNTs face significant challenges. The samples were obtained from one of my colleagues in the group. This master thesis focused on a thorough analysis of the optical properties of the materials. The samples corresponded to material purified through different processes. The samples used for this study were purified following 5 different protocols. **PT2** employing a mild acid treatment with HCl and H_2O_2 and annealed in air at 450°C for 30min.
For **PT3** and **PT4** a harsher acid treatment was used. The as-synthesized material was dispersed in 35ml of HNO_3 at 25°C and 80°C respectively and annealed in air at 450°C. For **Pc** a physical approach was used. The material was dispersed in DOC 2% and ultracentrifuged. Then the solution was filtered and then again dispersed and sonicated for $20min$. Then the solution was filtered and dispersed with methanol. Subsequently, the solution was filtered a third time and rinsed using hot water at $70°C$. This procedure was done four times, then the sample was dried at room temperature. For **P6** a combination of mild acid treatment and DGU was employed. The material was dispersed H_2O_2 30% and sonicated for $30min$, then washed and dissolved in HCl 37% and sonicated for $30min$ then washed with water and filtered using Millipore-Type-Jeep-$0.2nm$ and then dried. The dried material was annealed in air for 1h at 350°C. Subsequently, the material was dispersed in a $1.5\%DOC$ and $1.5\%SDS$ ($CH_3(CH_2)_{11}C_6H_4SO_3Na$) solution and ultracenrtrifuged at $50000RPMs$ for 2h. The supernatant was collected and washed in a millipore for several times.
The chemical purification method involving strong acids, HNO_3, demonstrated an I_D/I_G ratio of ~ 0.22 to ~ 0.36, while the DGU purification path showed a ratio of $I_D/I_G = 0.17$, indicating high-quality purified material. By comparing the purification pathways, the DGU method achieves the lowest reported damage index for CBx-SWNTs. Furthermore, a focus was the sorting of CBx-SWNTs by diameter and chirality. The DGU separation process utilizes a combination of surfactants to encapsulate and separate nanotubes with different diameters. The sorting process enhanced (6,5), (8,4), and (8,6), and it was also possible to obtain small diameter chiralities like (5,4), which exhibits stability close to the boundary limit of SWCNTs due to significant curvature effects[60], and (6,4).
The purification methods employed had a significant impact on the photoluminescence spectra of the SWCNTs. Acid treatments, such as HNO_3, effectively removed amorphous carbon and metal catalysts, leading to high PL intensities and a wide range of chirality distributions, particularly for species like (8,4), (6,5), and (8,6). However, harsher conditions, such as elevated temperatures, introduced defects, which could be the reason for the reduced PL intensity of some chiralities for the sample PT4. While the purification method for Pc resulted in the lowest damage index, indicating high material purity.

However, the PL intensity across all chiralities compared to the acid-treated samples is low. A reason for this could be that the acid-treated sample, despite annealing, still dispersed more effectively due to residual surface modifications, leading to more efficient sorting and a stronger PL response. The purification method applied to sample P6 and the chirality sorting via DGU resulted in a highly selective PL response, with strong signals observed only for the (6,5) and (8,3) chiralities. The initial oxidation with H_2O_2 introduced oxygen functional groups, which could have led to PL quenching. However, the subsequent treatments with HCl and annealing at 350°C successfully removed some of the defects. The sorting with DGU effectively isolating the chiralities (6,5) and (8,3). This purification and sorting process demonstrated the ability to selectively isolate certain chiralities while reducing others, in one purification and one sorting step. The consistent prominence of the chiralities (6,5), (8,4), (8,6), and (9,5) across all DGU-separated samples, despite differences in purification methods, suggests that these specific chiralities are highly abundant in the starting material and have similar buoyant densities in the surfactant environment used for separation. This clustering reflects the limitations of DGU in fully resolving overlapping density profiles. To realize the full potential of CBx-SWNTs for scalable applications, methods need to be develop for efficiently sorting them by their electronic and optical properties. Optimizing surfactant combinations or integrating techniques like DGU with selective functionalization or chromatography could enable more precise isolation of specific chiralities. Future research could focus on refining surfactant combinations or by combining various sorting techniques to improve chirality separation. Achieving effective, low-cost chirality sorting would significantly enhance material yield, advancing the feasibility of these nanotubes for large-scale commercial applications.

Bibliography

[1] Philip Kim Teri Wang Odom, Jin-Lin HUang and Charles M. Lieber. Structure and electronic properties of carbon nanotubes. *J.Phys.Chem. B* 104, 13, 2794-2809:88–95, February 15, 2000.

[2] A. H. Castro Neto, F. Guinea, N. M. R. Peres, K. S. Novoselov, and A. K. Geim. The electronic properties of graphene. *Rev. Mod. Phys.*, 81:109–162, Jan 2009.

[3] Simon Dubois, Zeila Zanolli, Xavier Declerck, and Jean-Christophe Charlier. Electronic properties and quantum transport in graphene-based nanostructures. *The European Physical Journal B*, 72:1–24, 11 2009.

[4] C. Thomsen J. Maultzsch S. reich. *Carbon Nanotubes: Basic Concepts and Physical properties.* WILEY-VCH Verlag GmbH Co.KGaA. Weinheim, 2004.

[5] R Bruce Wiseman and Shekhar Subramoney. Carbon nanotubes. *The Electrochemical Society interface*, 15(2):42–46, 2006.

[6] M.S. Dresselhaus, G. Dresselhaus, R. Saito, and A. Jorio. Raman spectroscopy of carbon nanotubes. *Physics reports*, 409(2):47–99, 2005.

[7] M.J. Longhurst and N. Quirke. The radial breathing mode of carbon nanotubes. *Molecular simulation*, 31(2-3):135–141, 2005.

[8] Ado Jorio, Riichiro Saito, G Dresselhaus, and M Dresselhaus. Determination of nanotubes properties by raman spectroscopy. *Philosophical transactions. Series A, Mathematical, physical, and engineering sciences*, 362:2311–36, 12 2004.

[9] L.M. Malard, M.A. Pimenta, G. Dresselhaus, and M.S. Dresselhaus. Raman spectroscopy in graphene. *Physics Reports*, 473(5):51–87, 2009.

[10] Sumio Iijima and Toshinari Ichihashi. Single-shell carbon nanotubes of 1-nm diameter. *Nature (London)*, 363(6430):603–605, 1993.

[11] Sumio Iijima. Helical microtubules of graphitic carbon. *Nature (London)*, 354(6348):56–58, 1991.

[12] Carlos Reinoso, Claudia Berkmann, Lei Shi, Alexis Debut, Kazuhiro Yanagi, Thomas Pichler, and Paola Ayala. Toward a predominant substitutional bonding environment in b-doped single-walled carbon nanotubes. *ACS omega*, 4(1):1941–1946, 2019.

[13] Paola Ayala, Raul Arenal, Annick Loiseau, Angel Rubio, and Thomas Pichler. The physical and chemical properties of heteronanotubes. *Reviews of modern physics*, 82(2):1843–1885, 2010.

[14] K. McGuire, N. Gothard, P.L. Gai, M.S. Dresselhaus, G. Sumanasekera, and A.M. Rao. Synthesis and raman characterization of boron-doped single-walled carbon nanotubes. *Carbon (New York)*, 43(2):219–227, 2005.

[15] D. L. Carroll, Ph Redlich, X. Blase, J. C. Charlier, S. Curran, S. Roth, P. M. Ajayan, and M. Rühle. Effects of nanodomain formation on the electronic structure of doped carbon nanotubes. *Physical review letters*, 81(11):2332–2335, 1998.

[16] G. Ruiz-Soria, S. Daothong, T. Pichler, and P. Ayala. Spectroscopic study of the diameter distribution of b-doped single-walled carbon nanotubes. *PHYSICA STATUS SOLIDI B-BASIC SOLID STATE PHYSICS*, 249(12):2469–2472, 2012.

[17] Paola Ayala, Wolfgang Plank, Alexander Grüneis, Esko I. Kauppinen, Mark H. Rümmeli, Hans Kuzmany, and Thomas Pichler. A one step approach to b-doped single-walled carbon nanotubes. *Journal of Materials Chemistry*, 18(46):5676–5681, 2008.

[18] Peng-Xiang Hou, Chang Liu, and Hui-Ming Cheng. Purification of carbon nanotubes. *Carbon (New York)*, 46(15):2003–2025, 2008.

[19] Marziyeh Karandish, Somayeh Fardindoost, and Gholamreza Pazuki. A novel approach in sorting chirality species of single-wall carbon nanotubes based on an aqueous two-phase system of polymer-salt. *Scientific reports*, 10(1):2025–2025, 2020.

[20] Hongbo Li and Qingwen Li. Selective separation of single-walled carbon nanotubes in solution. In *Electronic Properties of Carbon Nanotubes*. IntechOpen, 2011.

[21] F Bonaccorso, T Hasan, P. H Tan, C Sciascia, G Privitera, G Di Marco, P. G Gucciardi, and A. C Ferrari. Density gradient ultracentrifugation of nanotubes: Interplay of bundling and surfactants encapsulation. *Journal of physical chemistry. C*, 114(41):17267–17285, 2010.

[22] P. R. Wallace. Erratum: The band theory of graphite [phys. rev. 71, 622 (1947)]. *Physical review*, 72(3):258–258, 1947.

[23] Noriaki Hamada, Shin-ichi Sawada, and Atsushi Oshiyama. New one-dimensional conductors: Graphitic microtubules. *Phys. Rev. Lett.*, 68:1579–1581, Mar 1992.

[24] Riichiro Saito, Mitsutaka Fujita, G. Dresselhaus, and M. S. Dresselhaus. Electronic structure of graphene tubules based on c_{60}. *Phys. Rev. B*, 46:1804–1811, Jul 1992.

[25] E. Y Andrei, Guohong Li, A Luican, J. M. B Lopes dos Santos, A. H Castro Neto, A Reina, and J Kong. Observation of van hove singularities in twisted graphene layers. *Nature physics*, 6(2):109–113, 2010.

[26] J. W. Mintmire and C. T. White. Universal density of states for carbon nanotubes. *Phys. Rev. Lett.*, 81:2506–2509, Sep 1998.

[27] C. T White and J. W Mintmire. Density of states reflects diameter in nanotubes. *Nature (London)*, 394(6688):29–30, 1998.

[28] Riichiro Saito, Mildred S. Dresselhaus, Kazuyoshi Tanaka, and S Iijima. Optical properties of carbon nanotubes. In *Carbon Nanotubes and Graphene*, pages 77–98. Elsevier, United Kingdom, 2014.

[29] Jean-Christophe Blancon. *Optical absorption and electronic properties of individual carbon nanotubes*. Theses, Université Claude Bernard - Lyon I, October 2013.

[30] Claus Klingshirn. *Semiconductor*. Springer, Berlin [u.a.], 1995.

[31] C.I. Cabrera, D.A. Contreras-Solorio, and L. Hernández. Joint density of states in low dimensional semiconductors. *Physica E: Low-dimensional Systems and Nanostructures*, 76:103–108, 2016.

[32] Amit K. Bhojani, Shweta Singh, and Dheeraj K. Singh. *Saga and Developments of Raman Spectroscopy*, pages 1–15. Springer Nature Singapore, Singapore, 2024.

[33] Amit K. Bhojani, Shweta Singh, and Dheeraj K. Singh. *Resonant and Non-resonant Raman Spectroscopy.*, pages 17–51. Springer Nature Singapore, Singapore, 2024.

[34] J. Kürti, V. Zólyomi, A. Grüneis, and H. Kuzmany. Double resonant raman phenomena enhanced by van hove singularities in single-wall carbon nanotubes. *Phys. Rev. B*, 65:165433, Apr 2002.

[35] Zhonghua Yu and Louis Brus. (n, m) structural assignments and chirality dependence in single-wall carbon nanotube raman scattering. *Journal of Physical Chemistry B - J PHYS CHEM B*, 105, 06 2001.

[36] Angelo Armano and Simonpietro Agnello. Two-dimensional carbon: A review of synthesis methods, and electronic, optical, and vibrational properties of single-layer graphene. *C (Basel)*, 5(4):67, 2019.

[37] M.S Dresselhaus, A Jorio, R Saito, and JS Langer. Characterizing graphene, graphite, and carbon nanotubes by raman spectroscopy. *Annual review of condensed matter physics*, 1(1):89–108, 2010.

[38] H KUZMANY, W PLANK, M HULMAN, Ch KRAMBERGER, A GRÜNEIS, Th PICHLER, H PETERLIK, H KATAURA, and Y ACHIBA. Determination of swcnt diameters from the raman response of the radial breathing mode. *The European physical journal. B, Condensed matter physics*, 22(3):307–320, 2001.

[39] J. Maultzsch, H. Telg, S. Reich, and C. Thomsen. Radial breathing mode of single-walled carbon nanotubes: Optical transition energies and chiral-index assignment. *Physical Review B*, 72(20), November 2005.

[40] Shrilekha V. Sawant, Ashwin W. Patwardhan, Jyeshtharaj B. Joshi, and Kinshuk Dasgupta. Boron doped carbon nanotubes: Synthesis, characterization and emerging applications – a review. *Chemical engineering journal (Lausanne, Switzerland : 1996)*, 427:131616, 2022.

[41] Jae Yel Yi and J. Bernholc. Atomic structure and doping of microtubules. *Physical review. B, Condensed matter*, 47(3):1708–1711, 1993.

[42] Makoto Okano, Taishi Nishihara, Yasuhiro Yamada, and Yoshihiko Kanemitsu. Chemical doping-induced changes in optical properties of single-walled carbon nanotubes. *Japanese Journal of Applied Physics*, 53(5S1):5–1–05FD02–4, 2014.

[43] C. Reinoso, L. Shi, O. Domanov, P. Rohringer, T. Pichler, and P. Ayala. Very high boron-doping on single-walled carbon nanotubes from a solid precursor. *Carbon (New York)*, 140:259–264, 2018.

[44] O. Stephan, P. M. Ajayan, C. Colliex, Ph. Redlich, J. M. Lambert, P. Bernier, and P. Lefin. Doping graphitic and carbon nanotube structures with boron and nitrogen. *Science (American Association for the Advancement of Science)*, 266(5191):1683–1685, 1994.

[45] Gul Rahman, Zainab Najaf, Asad Mehmood, Salma Bilal, Anwar ul Haq Ali Shah, Shabeer Ahmad Mian, and Ghulam Ali. An overview of the recent progress in the synthesis and applications of carbon nanotubes. *C*, 5(1), 2019.

[46] Kinghong Kwok and Wilson K.S. Chiu. Growth of carbon nanotubes by open-air laser-induced chemical vapor deposition. *Carbon*, 43(2):437–446, 2005.

[47] H J Ceragioli, A C Peterlevitz, J C R Quispe, A Larena, M P Pasquetto, M A Sampaio, and V Baranauskas. Synthesis and characterization of boron-doped carbon nanotubes. *Journal of physics. Conference series*, 100(5):052029, 2008.

[48] Z. Wang, C.H. Yu, D.C. Ba, and J. Liang. Influence of the gas composition on the synthesis of boron-doped carbon nanotubes by ecr-cvd. *Vacuum*, 81(5):579–582, 2007.

[49] P. Ayala, M. H. Rümmeli, T. Gemming, E. Kauppinen, H. Kuzmany, and T. Pichler. Cvd growth of single-walled b-doped carbon nanotubes. *PHYSICA STATUS SOLIDI B-BASIC SOLID STATE PHYSICS*, 245(10):1935–1938, 2008.

[50] G. Ruiz-Soria, P. Ayala, S. Puchegger, H. Kataura, K. Yanagi, and T. Pichler. On the purification of cvd grown boron doped single-walled carbon nanotubes. *PHYSICA STATUS SOLIDI B-BASIC SOLID STATE PHYSICS*, 248(11):2504–2507, 2011.

[51] Carlos Alberto Reinoso Jerez. Purification, stability and bonding environments on b-doped single-walled carbon nanotubes : a study on the electronic and optical properties [doctoral dissertation, university of vienna], 2018.

[52] Yasumitsu Miyata, Kazuhiro Yanagi, Yutaka Maniwa, Takeshi Tanaka, and Hiromichi Kataura. Diameter analysis of rebundled single-wall carbon nanotubes using x-ray diffraction: Verification of chirality assignment based on optical spectra. *Journal of physical chemistry. C*, 112(41):15997–16001, 2008.

[53] Seok Ho Jeong, Ki Kang Kim, Seok Jin Jeong, Kay Hyeok An, Seung Hee Lee, and Young Hee Lee. Optical absorption spectroscopy for determining carbon nanotube concentration in solution. *Synthetic metals*, 157(13):570–574, 2007.

[54] R Bruce Weiseman and Shekhar Subramoney. Carbon nanotubes. *The Electrochemical Society Interface*, 15(2):42, jun 2006.

[55] G Dresselhaus, Mildred S Dresselhaus, and Riichiro Saito. Physical properties of carbon nanotubes. In *Physical Properties Of Carbon Nanotubes*. World Scientific Publishing Company, Singapore, 1998.

[56] Riichiro Saito and Mildred S. Dresselhaus. Chapter 5 - optical properties of carbon nanotubes. In *Carbon Nanotubes and Graphene*, pages 77–98. Elsevier Ltd, second edition edition, 2014.

[57] Un Jeong Kim, Clascidia A Furtado, Xiaoming Liu, Gugang Chen, and Peter C Eklund. Raman and ir spectroscopy of chemically processed single-walled carbon nanotubes. *Journal of the American Chemical Society*, 127(44):15437–15445, 2005.

[58] M Milnera, J Kurti, M Hulman, and H Kuzmany. Periodic resonance excitation and intertube interaction from quasicontinuous distributed helicities in single-wall carbon nanotubes. *Physical review letters*, 84(6):1324–1327, 2000.

[59] R. Bruce Weisman and Sergei M Bachilo. Dependence of optical transition energies on structure for single-walled carbon nanotubes in aqueous suspension: An empirical kataura plot. *Nano letters*, 3(9):1235–1238, 2003.

[60] Xiaojun Wei, Takeshi Tanaka, Naoto Akizuki, Yuhei Miyauchi, Kazunari Matsuda, Mari Ohfuchi, and Hiromichi Kataura. Single-chirality separation and optical properties of (5,4) single-wall carbon nanotubes. *Journal of physical chemistry. C*, 120(19):10705–10710, 2016.

[61] Bilu Liu, Hua Jiang, Arkady V. Krasheninnikov, Albert G. Nasibulin, Wencai Ren, Chang Liu, Esko I. Kauppinen, and Hui-Ming Cheng. Chirality-dependent reactivity of individual single-walled carbon nanotubes. *Small (Weinheim an der Bergstrasse, Germany)*, 9(8):1379–1386, 2013.